University of West Attica

School of Engineering

Department of Biomedical Engineering

MSc program "Biomedical Engineering and Technology"

How Deep Learning Image Reconstruction (DLIR) affects the optimization of image quality and dose reduction on Computed Tomography

Konstantinos Dimos

Registration Number: bmet17

Supervisor

Spiros Kostopoulos, Associate Prof.

Medisp Lab., Dept. of Biomedical Engineering, UNIWA

February 2024, Athens

The Three-Member Examination Committee

Supervisor		
Spiros Kostopoulos	Dimitris Glotsos	Panagiotis Liaparinos
Associate Professor	Professor	Associate Professor
Digitally signed by Spyridon Kostopoulos Date: 2024.03.08 14:36:20 +02'00'	Digitally signed by DIMITRIOS GKLOTSOS Date: 2024.03.11 12:41:06 +02'00'	Panagiotis Liaparinos Digitally signed by Panagiotis Liaparinos Date: 2024.03.11 15:54:14 +02'00'
Signature	Signature	Signature

DECLARATION BY THE AUTHOR OF THE DIPLOMA THESIS

The signatory Konstantinos Dimos of Vasileios and Olga, with registration number bmet17, student of the MSc Program “Biomedical Engineering and Technology” of the University of West Attica, I declare responsibly that:

"I am the author of this Diploma Thesis and any help I had for its preparation is fully recognized and referenced. Also, any sources from which I have used data, ideas, or words, whether exact or paraphrased, are listed in their entirety, with full reference to the authors, the publisher, or the journal, including any sources that may have been used by the internet. I also certify that this work has been written exclusively by me and is a product of intellectual property of both myself and the University of West Attica.

Violation of my above academic responsibility is an essential reason for the revocation of my diploma ".

Date: **31** / **1** / **2024**

Signature

CONTENTS

Abstract

The aim of this study is to investigate the influence of deep learning-based reconstruction (DLIR) on image quality across varying dose levels within a Chest-Abdomen-Pelvis (CAP) protocol using a 512-slice CT scanner and an advanced anthropomorphic phantom. Comparative analysis between DLIR, Adaptive Statistical Iterative Reconstruction (ASIR-V), and conventional Filtered BackProjection (FBP) reconstructions was conducted at normal, low, and ultra-low dose levels.

The CT scanner employed in this experiment is the Revolution APEX by GE HealthCare (Waukesha, WI, USA). The experiment involves the use of a dedicated CT whole-body phantom, the PBU-60 by Kyoto Kagaku. A quantitative analysis was conducted, comparing the FBP Normal Dose (ND) and various reconstruction algorithms across three distinct dose levels (normal, low and ultra-low dose) and chest/abdomen/pelvis regions. Furthermore, an additional quantitative assessment was included, using ASIR-V60% as a reference due to its widespread utilization, between ASIR-V90% and DLIR-H. Also, a qualitative analysis performed to evaluate the general image quality and overall contrast of ASIR-V60%, ASIR-V90% and DLIR-H. The evaluation was carried out in terms of Signal-to-Noise Ratio (SNR) and Contrast-to-Noise Ratio (CNR).

The results highlight the feasibility of a low-dose protocol and suggest the potential introduction of an experimental ultra-low-dose protocol for CAP. The proposed implementation relies on the use of a deep-learning-based image reconstruction algorithm, which aims to maintain image quality and contrast levels comparable to those typically observed with conventional reconstruction algorithms used in regular and low-dose protocols.

Keywords: ultra-low dose, deep learning image reconstruction, anthropomorphic phantom, image quality

Acknowledgements

Completing this diploma thesis has been a journey filled with invaluable support, guidance, and encouragement from individuals whom I am deeply grateful for.

I extend my sincerest appreciation to Dr Efstathios Despotopoulos, MD, MSc, whose insightful qualitative analysis greatly enriched the depth and credibility of this thesis. Your expertise and dedication have been instrumental in shaping the quality of this work.

I owe a debt of gratitude to my dedicated colleagues, whose unwavering support and collaborative spirit contributed immensely to the success of this thesis. Your valuable input and constructive feedback were pivotal in shaping its direction.

I wish to express my heartfelt thanks to Spyridon Kostopoulos, Associate Professor in the Department of Biomedical Engineering, University of West Attica, whose mentorship, wisdom, and continuous encouragement guided me through this academic pursuit. Your belief in my capabilities has been a driving force behind this accomplishment.

I am deeply appreciative of the support and guidance provided by my mentor and colleague, Dimosthenis E. Gkotsis, PhD. Your insights, encouragement, and shared experiences have been incredibly valuable throughout this journey.

I am also grateful for the support from Diagnostic Center "Euromedica Engkefalos" in Chalandri, Greece. Their granting of access to the state-of-the-art Revolution Apex CT 512 was instrumental in obtaining high-quality data for this thesis. Their commitment to advancing research in healthcare has significantly contributed to the outcomes of this study.

Furthermore, my heartfelt thanks to General Electric Healthcare for their generous provision of the anthropomorphic phantom pivotal in this study. Your support has played a crucial role in ensuring the success and accuracy of this research.

To all those who played a part, directly or indirectly, in shaping this thesis, your contributions are sincerely appreciated. This thesis stands as a testament to the collective support and encouragement I have received. Thank you all for being an integral part of this milestone.

1. Introduction

1.1 Computed Tomography historical review

Tomography, as a concept, represents a modern advancement in medical imaging. Before the advent of Computed Tomography (CT), human capability was limited to acquiring two-dimensional images of a specific anatomical region through the use of plain radiographs. The introduction of plain radiography was made by the discovery of X-rays in 1895 by Wilhelm Conrad Roentgen. [1] However, the CT system marked a groundbreaking achievement by becoming the first technology capable of capturing thin slices of body region, and enabling the creation of a three-dimensional perspective of the human body. [2]

Figure 1*:* The first CT system: Brain CT scanner and couch Unit by Electric and Musical Industries Limited (EMI) brain scanner, installed at the Atkinson Morley's Hospital, Wimbledon in 1971. Image by Science and Society Picture Library [3]. Copyright for research use only.

The pioneering CT system was developed by Sir Godfrey Newbold Hounsfield and Allan McLeod Cormack (Figure 1). In recognition of their groundbreaking invention, these two scientists were awarded the Nobel Prize in Medicine in 1979. This recognition underscored the transformative impact of CT technology on medical imaging, ushering in a new era of diagnostic capabilities and contributing

significantly to the advancement of healthcare. [2] The technical characteristics of CT systems of first-generation contains an x-ray tube producing a pencil (very thin) beam and a single detector receiving the radiation placed diametrically opposite. This detector-tube system is designed to move vertically along a specified axis, executing a sequential process of completing a row, followed by rotational repositioning to repeat the procedure. The images obtained by this system are like Figure 2.

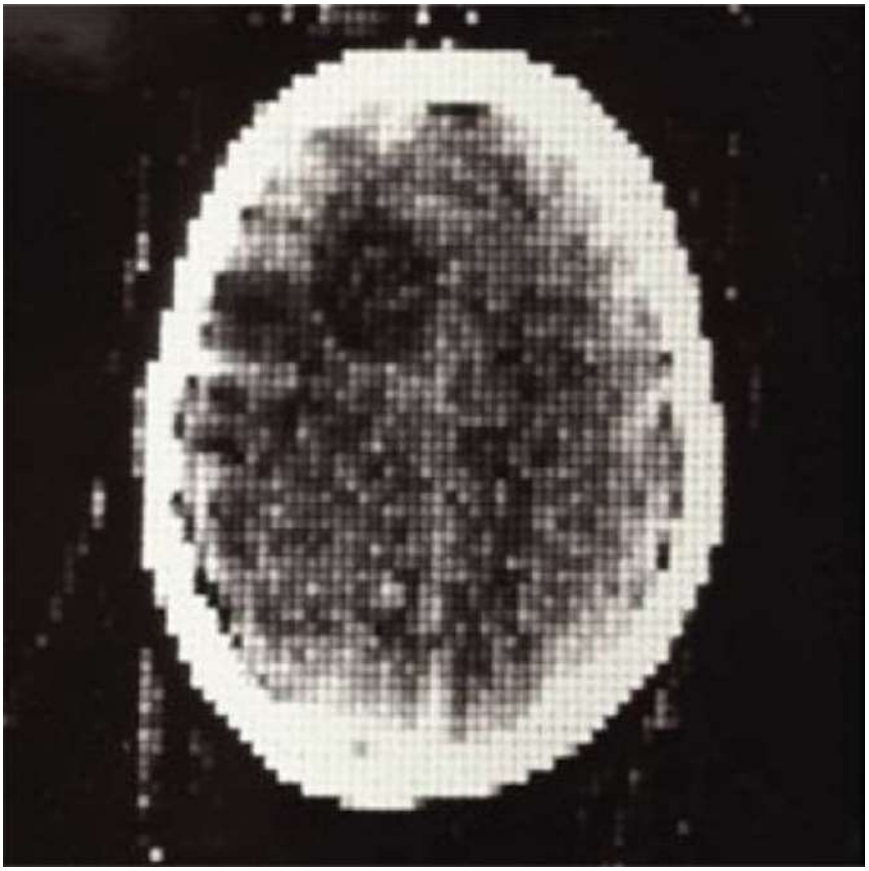

Figure 2: Image acquired by the first clinical CT brain scanner in October 1971 at Atkinson Morley's Hospital in London. A astrocytoma is visualized in anterior right lobe of the brain. Image from Science and Society Picture Library [2]. Copyright for research use only.

About second-generation CT systems as visualized on Figure 3 - B, contain multiple detectors for calculating multiple pencil beams created by the x-ray tube. The whole tube-detector systems also performed two motions one vertically, and when finish one slice, one rotationally but with multiple detectors. With this technique, the acquisition time reduced dramatically, for approximately 5 minutes of the first-generation for a slice and-approximately 25 min for brain scanning to approximately 20 seconds or a slice and 10 minutes for a brain scanning. With the third-generation (Figure 3 – C) CT scanners the one motion of tube-detector system removed and the

multiple pencil beams produced by the x-ray tube are replaced by a fan beam (thin in horizontal axis and wide in vertical axis). The whole systems only rotate around the examined area. [4] Third-generation CT scanners (Figure 3 – D) represent the widely adopted technology in contemporary medical imaging, and their prevalence endures to the present day. Nevertheless, ongoing advancements in techniques and features have been introduced to refine and enhance their capabilities, elevating their sophistication and overall developmental trajectory.

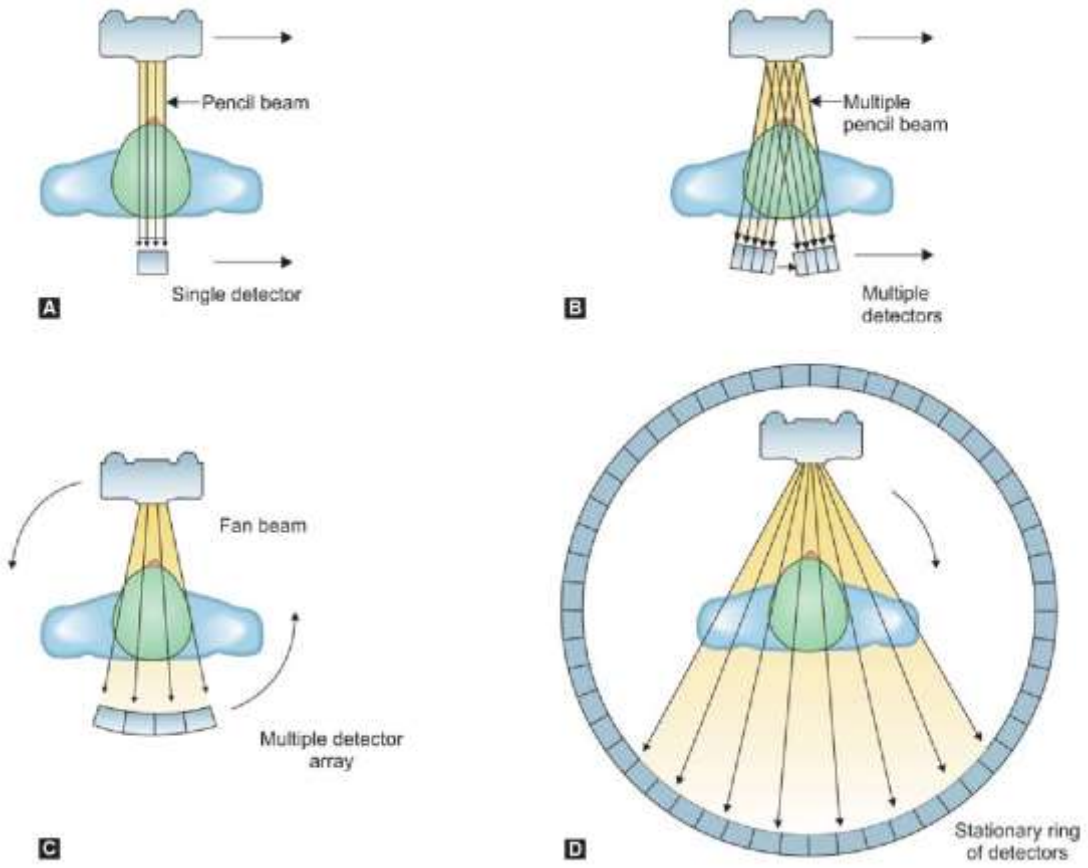

Figure 3: Schematic presentation of CT generations. (A) 1st generation: Pencil beam with single detector. (B) 2nd generation: pencil beam with multi detectors. (C) 3rd generation: fan beam with multi detector arch. (D) 4th generation: fan beam with stationary ring of detectors. Image directly from [7]

One of the most important advancements is spiral or helical technique which was introduced in 1990. (Figure 4) Spiral technique, as its name implies, is a spiral irradiation of the body results from the simultaneous movement of the bed and the tube-detector system. [5] Spiral acquisition facilitated a significant reduction in acquisition time and, for the first time, enabled complete coverage of certain organs within a single breath. This stands in stark contrast to the previously employed step-

and-shoot technique (or sequential), which invariably led to misregistration of anatomical details and overlapping images. [6]

The advancement of computational systems enabled the rapid processing of data from multiple slices. A significant milestone in this progression was the introduction of multi-slice CT. [4]. In 1998, the inaugural four-row detector system was introduced, signifying the capability to acquire data for a larger body region along the z-axis with fewer rotations of the tube-detector system. Since that time until the present, big manufacturers have achieved consistent advancements, culminating in the remarkable capability of obtaining up to 512 slices with a single rotation.

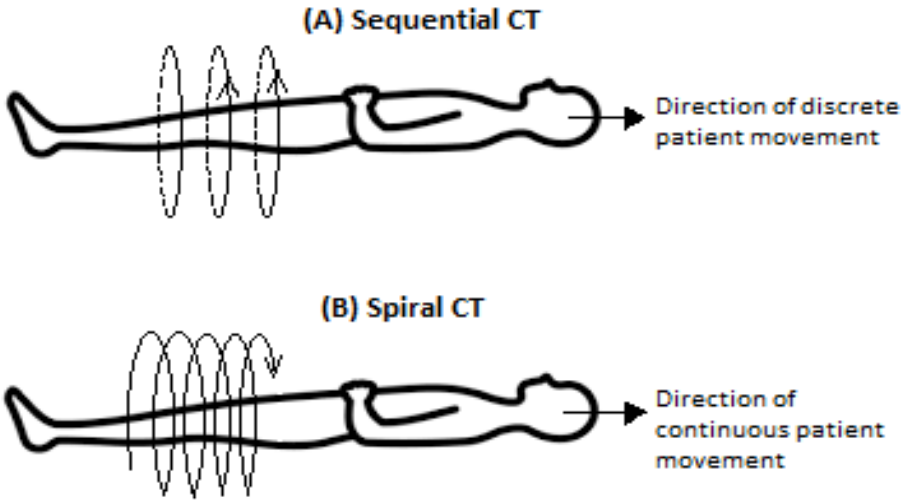

Figure 4: (A): Sequential acquisition or step-and-shoot technique. **(B)**: Spiral or helical acquisition. [8]

Finally, the fourth generation of CT systems was conceived with the goal of achieving even faster acquisition times. However, these systems proved unsuccessful in fulfilling their intended purpose, as they encountered numerous issues that had the unintended consequence of prolonging the divergence times of the received data. Consequently, manufacturers opted to advance the third-generation CT systems and abandoned the philosophy behind the fourth generation. [4]

1.2 Computed Tomography - General

Today, Computed Tomography (CT) is an important diagnostic medical imaging tool capable of providing valuable insights into a wide spectrum of different clinical scenarios. [9],[10]. It serves as a pivotal tool in the realm of clinical practice, fulfilling essential roles in routine health assessments, screening protocols, follow-up

examinations, and critical evaluations in emergency medical scenarios, among others Furthermore, in the recent era of the covid-19 pandemic, CT was proved extremely useful in the early diagnosis and management of the disease and became a front-line diagnostic examination, because it can facilitate the timely diagnosis, inform clinical decision-making, and track the progression of COVID-19. [11]

According to S. P. Power et al [12], in 2007, it was estimated that approximately 62 million CT scans are performed each year in the United States, significant increase to the roughly 3 million such exams conducted annually in 1980. Much like various fields of the medical field, employing CT scans entails a balance between advantages and drawbacks. Except the wide range of application, that mentioned above, CT also offers high-resolution imaging and generate three-dimensional reconstructions, enabling precise visualization of anatomical structures and their abnormalities. Additionally, contrast agents can be employed to enhance the visibility of specific tissues and augmenting diagnostic accuracy of the method.

However, while CT scans offer good contrast for many structures, they have limitations in distinguishing certain soft tissues compared to other imaging methods such as MRI, which provides more nuanced differentiation In addition, the most important limitation of CT is the radiation exposure to ionizing radiation. The effects of ionizing radiation have been widely recognized and comprehensively documented over many years [15]. In the realm of biology, ionizing radiation is known to induce cellular damage, posing a significant risk to DNA integrity and potentially culminating in mutations and carcinogenic outcomes. Furthermore, it can inflict tissue damage, with high doses leading to acute conditions such as radiation burns, radiation sickness, and severe injury to vital organs. The long-term consequences are substantial, as chronic exposure may significantly elevate the risk of cancer, cataract, and cardiovascular disease. Ionizing radiation also holds the potential to induce hereditary genetic mutations in reproductive cells, potentially impacting future generations. [15],[16].

The effective dose serves as a metric for quantifying ionizing radiation's potential to induce harm. It is denominated in sieverts (Sv), a unit that encompasses considerations such as the radiation type and the varying sensitivities of different tissues and organs to radiation exposure.

When the radiation dose is minimal, and particularly if it is administered gradually over an extended duration (characterized as a low dose rate), the associated risk substantially diminishes due to the increased probability of the body's capacity to repair radiation-induced damage. Nevertheless, it is important to acknowledge that there remains a risk of potential long-term consequences, such as cataracts or cancer, which may manifest years or even decades after exposure. Also, children and adolescents exhibit significantly heightened sensitivity to radiation compared to

adults, thereby implying a higher risk profile for this demographic group. In Table 1 is visualized some of the most usual CT examinations and corresponding dose level in mSv according to Radiology Society of North America (RSNA) [17]. It is clear that the dose level of CT examinations is at levels of a few tens of mSv maximum. Despite the low dose levels of CT, as already mentioned, remains a risk of potential long-term consequences.

Regarding the above, C-F Cao et al. [14] contact one of the biggest meta-analyses in order to estimate cancer risk by exposure to radiation under CT scanning conditions. Drawing from a sample of 111.6 million adult participants spanning three continents (Asia, Europe, and America), this meta-analysis reveals a substantial rise in cancer risks associated with CT scans among the adult population.

Table 1

CT Examinations and the corresponding average dose in mSv [17].

Computed Tomography Examination	Effective Dose (mSv)
Brain	1,6
Brain with contrast media	3,2
Chest	6,1
Coronary CT Angiography (heart)	8,7
Abdomen/Pelvis	7,7
Abdomen/Pelvis with contrast media	15,4
Lumbar Spine	1,4
Extremity	Less than 0,001

1.3 Dose Reduction

In light of the aforementioned considerations regarding radiation dose, it is imperative and of utmost significance to explore and implement strategies aimed at minimizing the radiation dose associated with CT scans. There are plenty of ways for dose reduction but it is imperative to maintain image quality to diagnostic levels and the trade-off between radiation dose and image quality should always be kept in mind of the healthcare professional. The rule that defines the dose level should always be guided by the A.L.A.R.A. (As Low As Reasonably Achievable) principle which describes that every examination should be utilized with as low as reasonably achievable (A.L.A.R.A.) dose [18].

Dose reduction is primarily accomplished through the manipulation of acquisition parameters that influence the overall beam quality. The principal irradiation parameters within a CT system include the potential difference to be developed in

the x-ray tube in kilovolts peak (kVp), the tube current in milliamperes (mA), the tube rotation speed or rotation time in milliseconds (msec), and the pitch, which denotes the ratio of table movement to the width of the X-ray beam, among others. Additionally, innovative tools have been developed to further enhance dose reduction in a more intelligent manner. One such tool is the Automatic Exposure Control (AEC), which modulates the tube current based on the size of the region being irradiated. [19].

In addition to achieving direct dose reduction through the explicit manipulation of the irradiation parameters, an indirect method that involves the utilization of advanced reconstruction algorithms. These algorithms enhance image quality beyond what is initially generated by the CT system's inherent reconstruction processes. Consequently, this approach enables the use of lower irradiation parameters while still attaining diagnostically satisfactory images of equal quality. This study aims to present a comparative analysis of the various reconstruction algorithms. Therefore, each of these algorithms will be examined in the subsequent subsections of this research.

1.4 CT image reconstruction

According to Lambert-Beer's Law (equation 1), when an X-ray beam traverses a patient, its intensity diminishes exponentially due to interactions with body's tissues [20]. Upon exiting the patient, the remaining X-ray photons are captured by the CT detector array and converted into digital signals. The attenuation of the X-ray beam along a specific path is determined by the sum of the product of the path length through each tissue (x) and the effective linear attenuation coefficient (μ) of that tissue, averaged over the X-ray spectrum. This is the line integral and the X-ray projection, also known as the attenuation profile, consists of a collection of line integrals taken along all the paths traversed by the X-ray beam.

$$I = I_0 \, e^{-\mu x} \quad (1)$$

Where:

I = the intensity of photons after passing through a material with some thickness x.

I_0 =the initial intensity of photons

e = Euler's Number

μ = the linear attenuation coefficient

x = distance traveled through a material (thickness)

In modern CT scans, X-ray projections are typically collected a thousand times during a 360° gantry rotation and are represented in a sinogram—a two-dimensional matrix that shows raw acquisition data as a function of gantry angle. Each point in the X-ray projections corresponds to a detector element along the detector row and exhibits a sinusoidal signal due to the coordinate's contribution at that angle (Figure 5). [21]

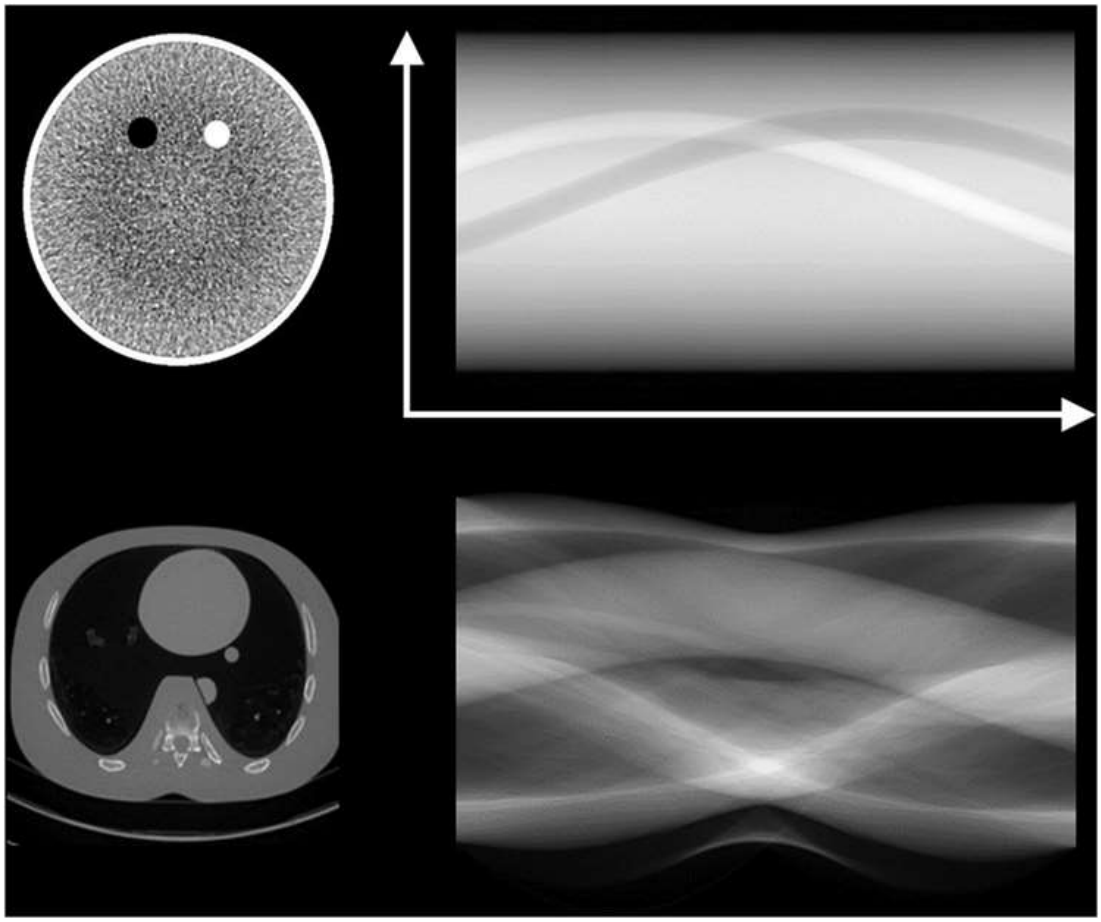

Figure 5: Top Left a CT image from a phantom with two different structures inside and top right the corresponding Sinogram. Bottom left image a Chest CT Image and bottom right the corresponding sinogram. Image sourced from [21]

1.5 Filtered Back Projection (FBP)

FBP reconstruction algorithm is the basic and most used reconstruction algorithm. In the simplest back-projection (BP), which is the first step of FBP, for each gantry angle the attenuation profile is effectively propagated back into the image space (Figure 6). The attenuation value within the sinogram undergoes division by the count of image pixels aligned along the pathway extending from the X-ray source to the detector. Consequently, the resultant average attenuation value is allocated to these specific

pixels. This procedure is repeated for every single gantry angle and as a result the reconstructed image is produced. [21] A simple back-projected image is much blurrier than what we have used for a regular CT image. In the FBP algorithm, before back-projection, projections undergo the application of a ramp filter. This filter functions as a high-pass filter. With the use of this high-pass filter the edges on the image are amplified and the blurriness is reduced effectively. [22]

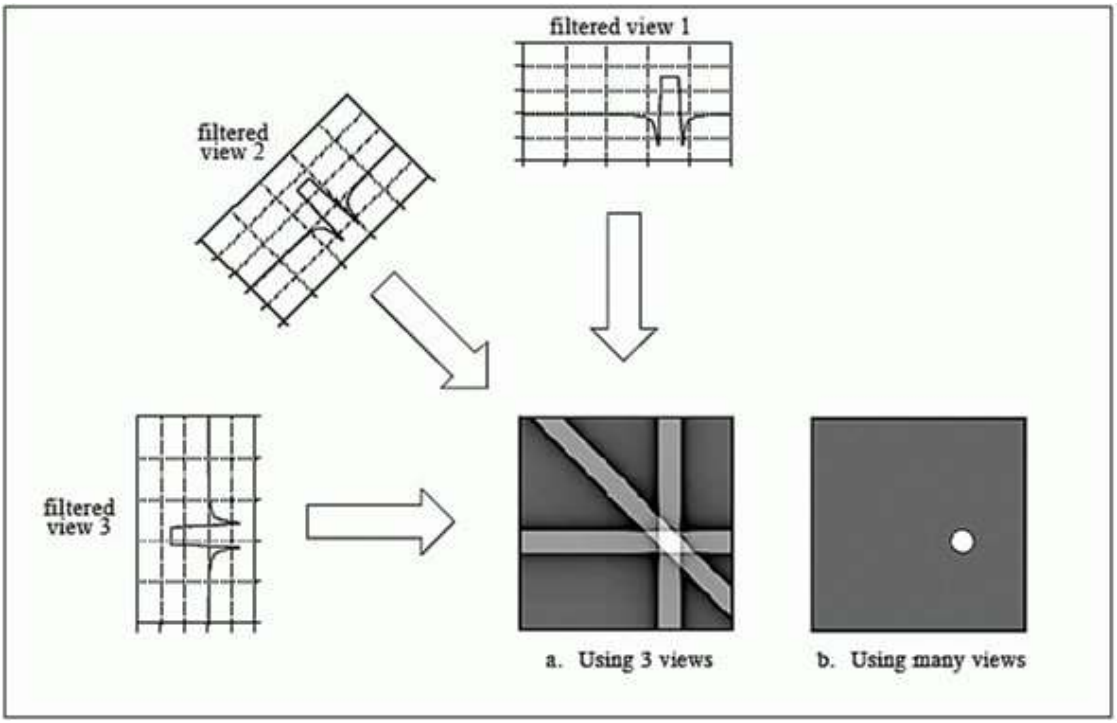

Figure 6: Filtered Back Projection schematic explanation. The visual content directly referenced in [23]

1.6 Iterative Reconstruction (IR)

Model-based Iterative Reconstruction (MBIR) algorithms produced by CT vendors in order improve Signal-to-Noise Ratio (SNR) and reduce radiation dose in relation to the use of FBP. In the case of IR algorithm, as its name defines, an iterative process in utilized in order to predict, define and correct noise without compromising important information (signal). In brief, MBIR uses sophisticated algorithms to simulate an anticipated image using statistical and optical models. MBIR is very efficient but requires long reconstruction time. A solution to that is the hybrid iterative reconstruction (HIR), also referred as statistical iterative reconstruction and partial model-based IR. By simply utilizing statistical system modeling and forward-projection steps, HIR offers a compromise between the MBIR and FBP (Figure 7). [24]

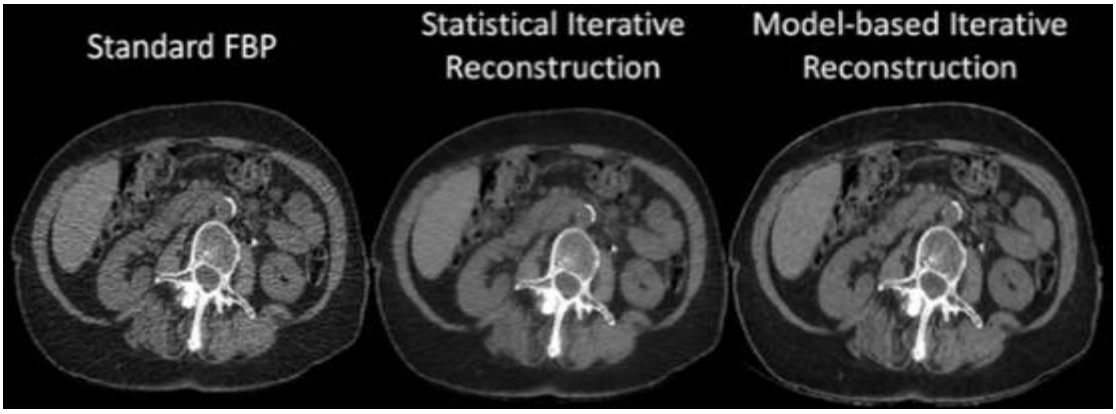

Figure 7: Three CT images of Upper Abdomen reconstructed with FBP (left), HIR/Statistical IR (middle) and MBIR (right). Figure directly from [24]

HIR algorithms start by using FBP images and then applies an extensive system of statistical models which tries to predict the noise and remove it. Specifically, an initial estimation of the observed item is established at the start of the image reconstruction. The initial estimation is then processed and revised in light of actual measured projections, earlier knowledge, or properties of the imaging equipment. Also, in order to optimize the image reconstruction process, iterative cycles frequently combine system optics, noise statistics, object, and physics models (for MBIR). The increase in spatial resolution of the reconstructed images is mostly attributable to the correct modeling of the system optics (Figure 8). The enhancement of low contrast detectability and the reduction of artifacts in the reconstructed images are mostly attributed to the correct modeling of the system noise statistics, object, and physics. Finally, the user can define how many times this circle of estimation, processing, and result of an image will be held based on their preferences for the image texture. A reduction in the number of iterative cycles leads to a higher degree of resemblance between the generated images and those obtained through the FBP technique, particularly with regard to noise reduction.[24] Consequently, when a user selects an Iterative Reconstruction (IR) algorithm with a setting of 0%, it signifies the production of images that closely mirror the characteristics of FBP-generated images. Nonetheless, multiple studies have demonstrated that when Iterative Reconstruction (IR) algorithms are employed at higher percentages, such as 90% to 100%, the resultant image tends to exhibit blurriness or “plastic texture” [30] , and in some cases also decrease the spatial resolution [30].

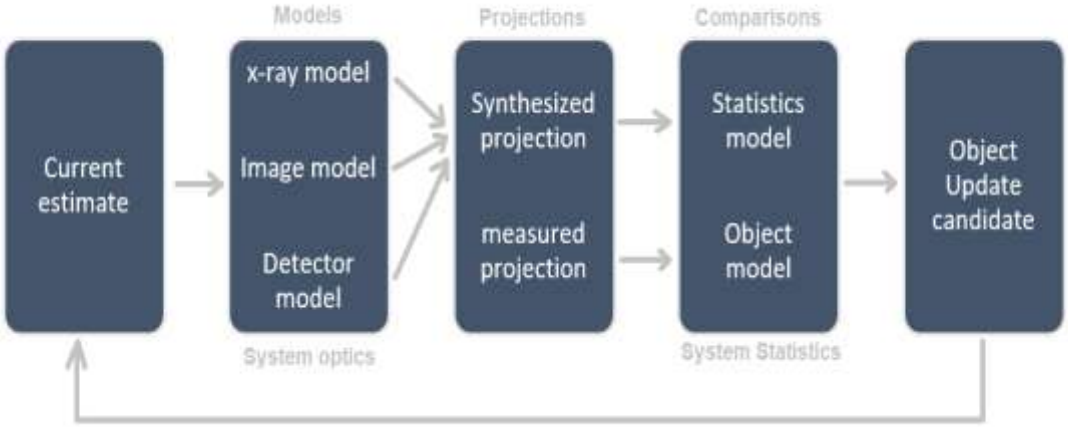

Figure 8: An MBIR inputs and data flow. The system optics includes a number of inputs from the X-ray characteristics (such as focusing spot), the image data (such as anatomy and geometry), and the detector (such as sampling). [24]

In conclusion, IR algorithms are very efficient and are able to reduce dose for CT examinations while maintain the image quality. Some examples of typical research about the efficiency of IR is the research of H. Kwon et al where 35% dose reduction was achieved compared with FBP for abdominal CT without reduction in image quality [26], and S. N. Patro, et al where the corresponding percentage is 36% for cervical spine CT protocol. [27]

In this study, a hybrid iterative reconstruction will be used, the Adaptive Statistical Iterative Reconstruction-V algorithm (ASiR-V) by GE HealthCare (Chicago, Illinois, United States of America) [28]. As the company has proved and mention, using ASiR-V instead of FBP can reduce patient's dose up to 82% while maintain the image quality on the same levels. Also, as GE HealthCare mentions on the official documentation about this algorithm, the corresponding percentage considering low-contrast detectability can reach 135%. [28]

1.7 Artificial Intelligence and Deep Learning

Deep Learning (DL) is a subcategory of Machine Learning (ML), both of which fall under the umbrella term of Artificial Intelligence (AI). Generally, ML focuses on the development of algorithms and models that enable computers to learn from and make predictions based on data that have been introduced to the system by humans. While this concept has been in existence for several years, it is only in recent years that humans have developed computers with sufficient strength to effectively process and manipulate vast amounts of data. This advancement has

enabled the creation of algorithms that demonstrate functionality in this context. So, the primary goal of machine learning is to create systems that can automatically improve their performance over time without being explicitly programmed. [48] Unlike conventional programming, where humans provide explicit instructions for computer tasks, machine learning relies on the system learning (as its name states) from data patterns which enables the system to generalize its knowledge. [48] Recently, AI has demonstrated strong abilities in solving multiple problems humanity had for decades and could not overtake. [36] The problem of image reconstruction, as mentioned before, is the triplet of high image quality with reduction of radiation dose and simultaneously fast reconstruction time, as reconstruction algorithms must exhibit swiftness to promptly render the data for precise and efficient examination. [31]

Deep Learning-based image reconstruction algorithms introduced the last years have proved that this is more than possible and even reduce dose in levels of plain radiography in some cases. [32] The Deep Learning- based Image Reconstruction (DLIR) is trained exactly as a human brain trained by repetition. An essential distinction between past and current DL algorithms is that contemporary DL algorithms are pre-programmed before implementation, solely when configured by the programmer. The essence of AI in this context is that DL algorithms autonomously learn how to predict and enhance noise removal through their Convolutional Neural Network (CNN), similarly to the way the human brain operates with its biological neural network. [34]

1.7.1 Deep Learning-based Image Reconstruction (DLIR)

The DLIR has a very complex and sophisticated way of operation and requires a huge number of data that have to be used in order to create a solid result. Specifically, thousands of pairs of images from a large database are introduced into a high-performance computer. Each pair of images consists of one low dose and low-quality image and the corresponding high dose and very high quality one. Then the system uses a CNN in order to find the mappings between the two image sets. A typical CNN is structured with layers that systematically convert input images into specified outcomes, acquiring increasingly advanced visual characteristics in the process. Starting with an initial image, the concealed layers of CNNs typically involve convolution and pooling operations to extract feature maps and amalgamate features, respectively. [49]

In the end of the process, given that the system has matched low-quality images with high-quality images on multiple occasions, it no longer necessitates the coexistence of both types to generate high-quality images (Figure 9). Consequently, the system is now capable of producing high-quality images exclusively from low-quality inputs. In other words, with DLIR it is possible to provide high quality images

by using very low radiation and in clinical acceptable time as the algorithm is not trained on the scanning process but has undergone prior training. It is important to notice that this kind of AI reconstruction algorithms, in order to obtain approval for clinical use, are pushed to their limits as tested in multiple and very extreme cases for assessing their stable operation. [31] [33] [34]

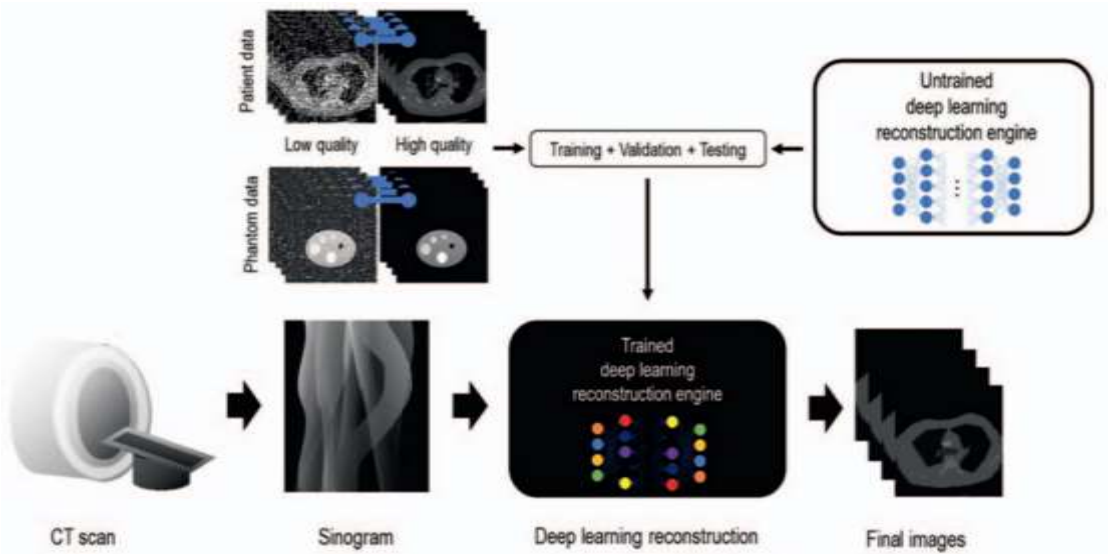

Figure 9: DLIR schematic steps. The image obtained from citation [34]

2. Material and Methods

2.1 Material

The CT scanner employed in this experiment is the Revolution APEX (Figure 10), a product of GE HealthCare (Waukesha, WI, USA). The central feature of the CT scanner used for this experiment is the implementation of TrueFidelity™, a Deep Learning-based image reconstruction method. Additionally, the scanner boasts a maximum 1,300 mA X-ray output, a rotation speed of 0.28 seconds per rotation, and a 160 mm z-coverage in a single axial exposure.

Figure 10: General Electric Healthcare Revolution APEX CT system in Euromedica Engefalos in Chalandri, Greece. Picture from personal archive.

Figure 11: PBU-60 Whole body phantom as placed for the Chest/Abdomen/Pelvis irradiation with the arms raised as in actual patient positioning**.** Picture from personal archive.

Furthermore, the experiment involves the use of a dedicated CT whole-body phantom, the PBU-60 by Kyoto Kagaku, renowned for its widespread application in medical imaging for whole-body CT scanner quality assurance and performance evaluation (Figure 11). According to the manufacturer, is designed to mimic the average human body's anatomical features, including bones, soft tissues, and organs, allowing for comprehensive evaluation of the scanner's imaging capabilities across different body regions. Notably, the phantom's tissue-equivalent materials closely mirror human tissue in terms of X-ray attenuation, facilitating precise evaluations of image quality, dose distribution, and spatial resolution across various tissue types, as specified by the manufacturer."

2.2 Methods

2.2.1 Image acquisition

The selected body region for this experiment is the Chest/Abdomen/Pelvis (CAP), chosen for its widespread clinical relevance [35] and the diversity of organs and tissues it encompasses. This combination of examinations is commonly performed in clinical settings, making it an ideal choice for the assessment, owing to the intricate interplay of various physiological structures. Its inclusion promises to render the evaluation more comprehensive and insightful, given the complexity and critical

diagnostic value of this particular body region. The parameters used for the irradiation are show in Table 2.

Two out of the three protocols, namely Normal and Low Dose, were acquired to align with the standard procedures practiced in the clinical department. The third protocol, Ultra Low Dose, was exclusively obtained for the purpose of evaluating the performance of the three reconstruction methods. A notable divergence between the experimental data acquisition and the clinical protocols lies in the exclusion of dose modulation during the experimental data acquisition, ensuring the feasibility of a meaningful comparison between the reconstruction methods. Notably, the tube current was precisely adjusted to correspond with the Noise Index for each respective protocol.

Table 2

Detailed parameters for data acquisition and image reconstruction for all dose levels.

Radiation Dose Levels	Normal Dose	Low Dose	Ultra Low Dose
$CTDI_{vol}$ (mGy)	4,44mGy	2,46	1,34
Parameters			
kVp	80	80	80
mA	180	100	55
Scan Field of View (SFOV)	Medium Body	Medium Body	Medium Body
Scan type	helical	helical	helical
Rotation time	0.5s	0.5s	0.5s
Detector coverage	80mm	80mm	80mm
Pitch	0,508:1	0,508:1	0,508:1
Coverage speed	81,25mm/s	81,25mm/s	81,25mm/s
Slice Thickness	2.5mm	2.5mm	2.5mm
Reconstruction Type	Standard	Standard	Standard
Reconstruction Mode	Helical Plus	Helical Plus	Helical Plus
Interval	2.5mm	2.5mm	2.5mm
Reconstruction Method	FBP, ASIR-V30%, 60%, 90%, DLIR-L, M, H	FBP, ASIR-V30%, 60%, 90%, DLIR-L, M, H	FBP, ASIR-V30%, 60%, 90%, DLIR-L, M, H

2.2.2 Image processing

The evaluation metrics encompass Signal-to-Noise Ratio (SNR) and Contrast-to-Noise Ratio (CNR), with all measurements extracted from the Picture Archiving and Communication System (PACS). Signal-to-Noise Ratio (SNR) serves as a crucial metric

for quantifying the noise level within an imaging system, and it is determined using the following formula

$$SNR = \frac{HU_{tissue}}{SD_{tissue}} \quad (2)$$

where HU_{tissue} represents the mean Hounsfield Unit (HU) value within the designated Region of Interest (ROI), and SD_{tissue} denotes the corresponding standard deviation. In the context of this experiment's Chest/Abdomen/Pelvis (CAP) assessment, distinct ROIs were employed for each specific region, as shown in Figure 12. The chest images underwent evaluation with five Regions of Interest (ROIs) placed within the homogeneous left and right lung parenchyma of the phantom. For abdominal assessment, five ROIs were positioned on the homogeneous liver parenchyma. Pelvic evaluation involved four ROIs placed on the urinary bladder, enabling specific and precise assessments for each region. It's crucial to emphasize that in each distinct data acquisition at different dose levels, the ROIs were consistently placed using workstation tools rather than manual methods. This meticulous approach ensures standardized ROI positioning across varying doses, facilitating a reliable comparison and allowing for a comprehensive assessment of how dose variation impacts measured metrics. This method also aids in accurately evaluating the system's performance.

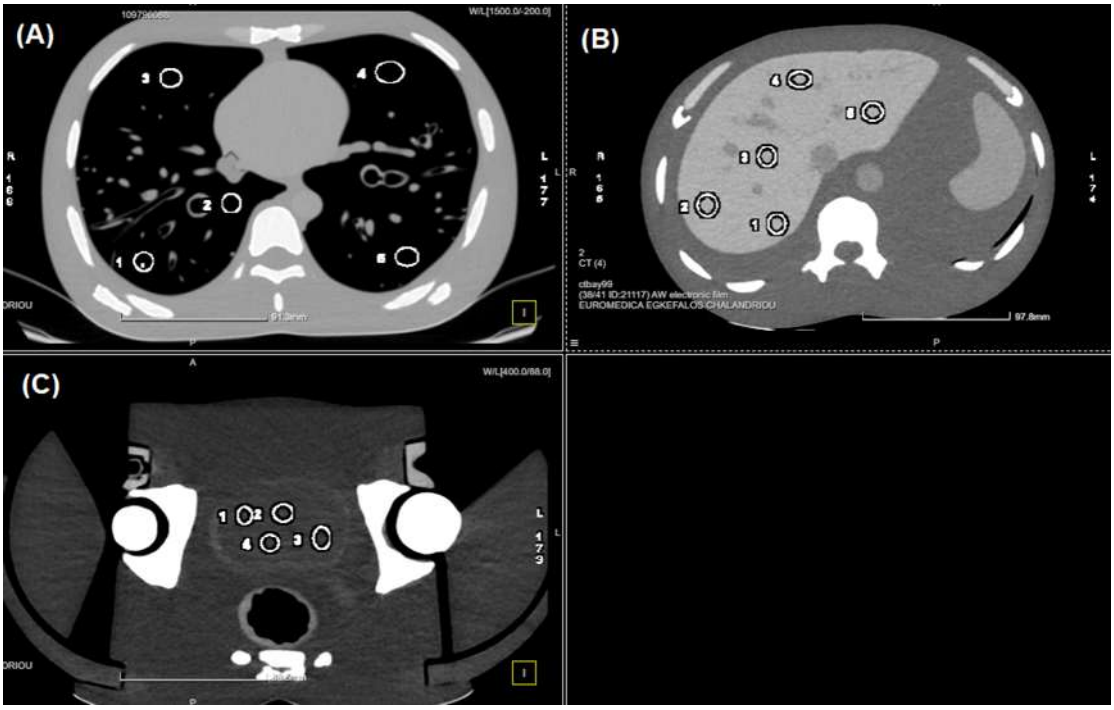

Figure 12: ROIs placement for SNR quantification. (A) Chest, (B) Abdomen, and (C) Pelvis

Similar to the process involved in the SNR calculation, distinct calculations were performed for each specific body region for the Contrast-to-Noise Ratio (CNR). The formula used for CNR calculation is the following

$$CNR = \frac{HU_{tissue} - HU_{background}}{SD_{background}} \quad (3)$$

where HU_{tissue} represents the mean Hounsfield Unit (HU) value within the tissue region of interest, $HU_{background}$ denotes the mean HU value within the background region, and $SD_{background}$ represents the standard deviation of the HU values in the background region. This formula enables the quantitative assessment of the CNR, providing valuable insights into the contrast and noise characteristics within the imaging data. This approach ensured tailored assessments for the chest, abdomen, and pelvis regions, allowing for an accurate and comprehensive evaluation of the contrast and noise characteristics pertinent to each anatomical area.

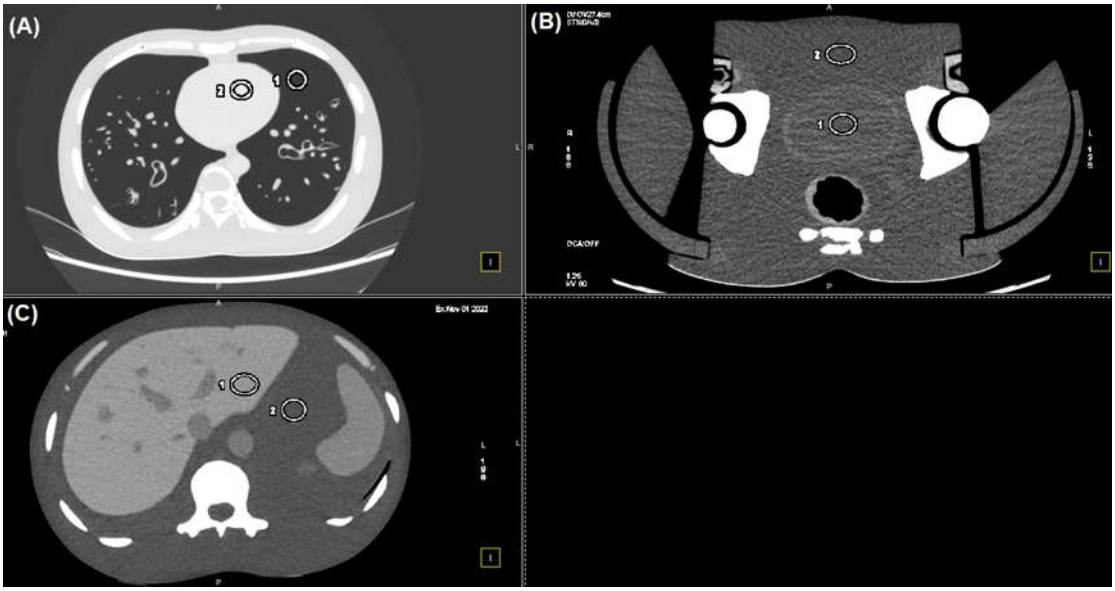

Figure 13: ROIs placement for CNR quantification at (A): Chest. ROI 1 placed on upper lobe of left lung and ROI 2 placed on left ventricle of the heart, (B): Pelvis. ROI 1 placed on urinary bladder and ROI 2 placed on abdominal fat, and (C): Abdomen. ROI 1 placed on liver parenchyma and ROI 2 placed on abdominal fat.

Let CNR_{Chest} denote the Contrast-to-Noise Ratio for the Chest assessment, which is calculated based on the Regions of Interest (ROIs) placed on the upper lobe of the left lung parenchyma (considered as the tissue) and on the left ventricle of the heart (considered as the background).

Similarly, let $CNR_{Abdomen}$ denote the Contrast-to-Noise Ratio for the Abdomen assessment, calculated based on the ROIs placed on the liver parenchyma (considered as the tissue) and the abdominal fat (considered as the background).

Moreover, let CNR_{Pelvis} denote the Contrast-to-Noise Ratio for the Pelvis assessment, calculated based on the ROIs placed on the urinary bladder (considered as the tissue) and the abdominal fat (considered as the background). These assessments are illustrated in Figure 13.

2.2.3 Quantitative analysis

For the statistical analysis, SNR calculations were derived from multiple Regions of Interest (ROIs) as illustrated in Figure 12 (5 ROIs in chest, 5 in abdomens and 4 in pelvis). This encompassed three distinct dose levels and seven different reconstruction algorithms (FBP, ASIR30%, ASIR60%, ASIR90%, DLIR Low, DLIR Medium, and DLIR High), resulting in a total of 189 SNR estimations.

To assess the normality of the data distribution, a Shapiro-Wilk test was performed.

Following confirmation of normality, the initial analysis involved conducting paired t-tests. In case where normality did not met, the Wilcoxon non parametric test was utilized. These tests were conducted between the FBP Normal Dose and each of the other reconstruction algorithms within all three dose levels for every specific anatomical region. A total of 54 t-tests were conducted, with 18 tests executed for each specific body region. These analyses encompassed the calculation of p-values, comparing various reconstruction algorithms against the FBP Normal Dose across all three dose levels within each anatomical region.

For an additional analysis, three reconstruction algorithms demonstrating the highest SNR and CNR rates were selected: ASIR60%, ASIR90%, and DLIR High. ASIR60% was designated as the reference point. Subsequently, paired t-tests were conducted for each body region, comparing ASIR60% against the other two reconstruction algorithms—ASIR90% and DLIR High—at every dose level within the respective anatomical regions.

2.2.4 Qualitative analysis

For qualitative analysis, images characterized by the highest Signal-to-Noise Ratio (SNR) and Contrast-to-Noise Ratio (CNR) are selected to further assess their alignment with the daily evaluations conducted by medical professionals. To this end, a radiologist with over 25 years of experience evaluated a total of 27 regions employing various reconstruction methods and across different dose levels.

Specifically, across three dose levels—Normal, Low, and Ultra Low—the radiologist assessed chest, upper abdomen, and pelvis images reconstructed using ASIR60%, ASIR90%, and DLIR High. This comparative assessment occurred within an advanced

workstation environment. The radiologist conducted evaluations on three image series within the same dose level and region (e.g., normal dose, chest) using the three distinct reconstruction methods (ASiR 60%, ASiR 90%, and DLIR H) without prior knowledge of their origin.

The assessment process involved responding to two questions: the first regarding general image quality and the second pertaining to image contrast. Ratings were marked on a scale from 1 (very poor) to 5 (excellent) for each question.

3. Results

3.1 Quantitative analysis results

3.1.1 SNR Results

Tables 3, 4, and 5 specifically present the tabulated average SNR calculations for the chest, abdomen, and pelvis regions, respectively. These tables comprehensively outline the SNR values corresponding to each reconstruction algorithm at the three different dose levels employed—normal, low, and ultra-low doses—within their corresponding anatomical regions. Furthermore, in the Appendix are presented in detail all ROIs SNRs for each body region and dose level

Table 3:

Chest SNR Average of 5 ROIs Results

Reconstruction Algorithm	Normal Dose SNR	Low Dose SNR	Ultra Low Dose SNR
FBP	80,3	67,8	56,0
ASIR-V30%	103,9	82,2	66,7
ASIR-V60%	143,5	108,0	84,6
ASIR-V90%	216,9	152,4	115,6
DLIR Low	109,5	88,8	71,2
DLIR Medium	141,4	115,4	90,5
DLIR High	201,6	163,7	125,6

Table 4:

Abdomen SNR Average of 5 ROIs Results

Reconstruction Algorithm	Normal Dose SNR	Low Dose SNR	Ultra Low Dose SNR
FBP	2,7	2,2	1,9
ASIR-V30%	3,6	2,8	2,4
ASIR-V60%	5,1	3,9	3,4
ASIR-V90%	8,5	6,1	5,2
DLIR Low	4,4	3,8	3,5
DLIR Medium	5,4	4,9	4,5

DLIR High	7,2	7,2	6,6

Table 5:

Pelvis SNR Average of 5 ROIs Results

Reconstruction Algorithm	Normal Dose SNR	Low Dose SNR	Ultra Low Dose SNR
FBP	0,587	0,446	0,609
ASIR-V30%	0,738	0,569	0,754
ASIR-V60%	1,017	0,781	0,997
ASIR-V90%	1,533	1,316	1,409
DLIR Low	0,916	0,786	0,985
DLIR Medium	1,102	0,999	1,216
DLIR High	1,403	1,377	1,603

3.1.2 Statistical analysis results – FBP Normal Dose as reference

Statistical analysis results comparing the Signal-to-Noise Ratio (SNR) of the FBP algorithm in the Normal Dose level with other algorithms across all three dose levels (Low, Normal, and High) are presented in Tables 6, 7, and 8 for the Chest, Abdomen, and Pelvis body regions, respectively. The third column of each table presents the corresponding p-values, providing a measure of statistical significance for the observed differences in SNR between the algorithms at various dose levels and body regions. All the results which p-values exceed 0,05 are colored red.

Table 6

SNR Comparison: FBP Algorithm (Normal Dose) vs. Others - <u>Chest</u>

Reconstruction algorithm 1	Reconstruction algorithm 2	*P* value
FBP Normal Dose	ASIR30% Normal Dose	0,018
FBP Normal Dose	ASIR60% Normal Dose	<.001
FBP Normal Dose	ASIR90% Normal Dose	0,008
FBP Normal Dose	DLIR-L Normal Dose	0,006
FBP Normal Dose	DLIR-M Normal Dose	<.001
FBP Normal Dose	DLIR H Normal Dose	0,008
FBP Normal Dose	FBP Low Dose	0,019

FBP Normal Dose	ASIR30% Low Dose	0,70
FBP Normal Dose	ASIR60% Low Dose	0,002
FBP Normal Dose	ASIR90% Low Dose	<.001
FBP Normal Dose	DLIR-L Low Dose	0,16
FBP Normal Dose	DLIR-M Low Dose	<.001
FBP Normal Dose	DLIR H Low Dose	<.001
FBP Normal Dose	FBP Ultra Low Dose	<.001
FBP Normal Dose	ASIR30% Ultra Low Dose	0,015
FBP Normal Dose	ASIR60% Ultra Low Dose	0,403
FBP Normal Dose	ASIR90% Ultra Low Dose	<.001
FBP Normal Dose	DLIR-L Ultra Low Dose	0,093
FBP Normal Dose	DLIR-M Ultra Low Dose	0,108
FBP Normal Dose	DLIR H Ultra Low Dose	<.001

Table 7

SNR Comparison: FBP Algorithm (Normal Dose) vs. Others - Abdomen

Reconstruction algorithm 1	Reconstruction algorithm 2	p value
FBP Normal Dose	ASIR30% Normal Dose	<.001
FBP Normal Dose	ASIR60% Normal Dose	<.001
FBP Normal Dose	ASIR90% Normal Dose	<.001
FBP Normal Dose	DLIR-L Normal Dose	0,008
FBP Normal Dose	DLIR-M Normal Dose	0,008
FBP Normal Dose	DLIR H Normal Dose	0,008
FBP Normal Dose	FBP Low Dose	<.001
FBP Normal Dose	ASIR30% Low Dose	0,640
FBP Normal Dose	ASIR60% Low Dose	<.001
FBP Normal Dose	ASIR90% Low Dose	<.001
FBP Normal Dose	DLIR-L Low Dose	<.001
FBP Normal Dose	DLIR-M Low Dose	0,008
FBP Normal Dose	DLIR H Low Dose	0,008
FBP Normal Dose	FBP Ultra Low Dose	<.001

FBP Normal Dose	ASIR30% Ultra Low Dose	0,049
FBP Normal Dose	ASIR60% Ultra Low Dose	0,016
FBP Normal Dose	ASIR90% Ultra Low Dose	<.001
FBP Normal Dose	DLIR-L Ultra Low Dose	<.001
FBP Normal Dose	DLIR-M Ultra Low Dose	0,008
FBP Normal Dose	DLIR H Ultra Low Dose	0,008

Table 8

SNR Comparison: FBP Algorithm (Normal Dose) vs. Others - Pelvis

Reconstruction algorithm 1	Reconstruction algorithm 2	p value
FBP Normal Dose	ASIR30% Normal Dose	0,227
FBP Normal Dose	ASIR60% Normal Dose	0,038
FBP Normal Dose	ASIR90% Normal Dose	0,017
FBP Normal Dose	DLIR-L Normal Dose	0,044
FBP Normal Dose	DLIR-M Normal Dose	0,013
FBP Normal Dose	DLIR H Normal Dose	0,003
FBP Normal Dose	FBP Low Dose	0,101
FBP Normal Dose	ASIR30% Low Dose	0,825
FBP Normal Dose	ASIR60% Low Dose	0,073
FBP Normal Dose	ASIR90% Low Dose	0,022
FBP Normal Dose	DLIR-L Low Dose	0,069
FBP Normal Dose	DLIR M Low Dose	0,008
FBP Normal Dose	DLIR- H Low Dose	0,003
FBP Normal Dose	FBP Ultra Low Dose	0,87
FBP Normal Dose	ASIR30% Ultra Low Dose	0,32
FBP Normal Dose	ASIR60% Ultra Low Dose	0,08
FBP Normal Dose	ASIR90% Ultra Low Dose	0,06
FBP Normal Dose	DLIR-L Ultra Low Dose	0,06
FBP Normal Dose	DLIR-M Ultra Low Dose	0,019
FBP Normal Dose	DLIR-H Ultra Low Dose	0,008

3.1.3 Statistical analysis results – ASIR-V60% Normal Dose as reference

The subsequent Tables 9, 10, and 11 present the derived p-values resulting from the comparison of the Signal-to-Noise Ratio (SNR) of ASIR-V60% between ASIR-V90% and DLIR High. ASIR60% serves as the benchmark among the three most proficient algorithms in performance. All the results which p-values exceed 0,05 are colored red.

Table 9

SNR Comparison: ASIR-V60% (Normal Dose) vs. ASIR-V90% and DLIR-H in all dose levels - Chest

Reconstruction algorithm 1	Reconstruction algorithm 2	p value
ASIR60 Normal Dose	ASIR90 Normal Dose	0,013
ASIR60 Normal Dose	DLIR-H Normal Dose	0,011
ASIR60 Normal Dose	ASIR90 Low Dose	0,53
ASIR60 Normal Dose	DLIR-H Low Dose	0,22
ASIR60 Normal Dose	ASIR90 Ultra Low Dose	0,05
ASIR60 Normal Dose	DLIR-H Ultra Low Dose	0,19

Table 10

SNR Comparison: ASIR-V60% (Normal Dose) vs. ASIR-V90% and DLIR-H in all dose levels - Abdomen

Reconstruction algorithm 1	Reconstruction algorithm 2	p value
ASIR60 Normal Dose	ASIR90 Normal Dose	0,002
ASIR60 Normal Dose	DLIR-H Normal Dose	<.001
ASIR60 Normal Dose	ASIR90 Low Dose	0,056
ASIR60 Normal Dose	DLIR-H Low Dose	<.001
ASIR60 Normal Dose	ASIR90 Ultra Low Dose	0,936
ASIR60 Normal Dose	DLIR-H Ultra Low Dose	0,004

Table 11

SNR Comparison: ASIR-V60% (Normal Dose) vs. ASIR-V90% and DLIR-H in all dose levels - Pelvis

Reconstruction algorithm 1	Reconstruction algorithm 2	p value
ASIR60 Normal Dose	ASIR90 Normal Dose	0,16
ASIR60 Normal Dose	DLIR-H Normal Dose	0,13
ASIR60 Normal Dose	ASIR90 Low Dose	0,26
ASIR60 Normal Dose	DLIR-H Low Dose	0,14
ASIR60 Normal Dose	ASIR90 Ultra Low Dose	0,26
ASIR60 Normal Dose	DLIR-H Ultra Low Dose	0,09

3.2 Qualitative analysis results

Table 12 presents the outcomes of the qualitative analysis, delineating the evaluations of general image quality and contrast provided by a radiologist with 25 years of experience. Diagrams 1 and 2 present the mean evaluations of each reconstruction algorithm across the entirety of the Chest/Abdomen/Pelvis region and encompassing all dose levels.

Table 12

Region and dose level	Reconstruction algorithm	Evaluation criteria	Score
Normal Dose Chest	ASIR-V60%	Image quality	4
		Contrast	4
Normal Dose Chest	ASIR-V90%	Image quality	4
		Contrast	4
Normal Dose Chest	DLIR High	Image quality	4
		Contrast	4
Normal Dose Abdomen	ASIR-V60%	Image quality	4
		Contrast	4
Normal Dose Abdomen	ASIR-V90%	Image quality	4
		Contrast	3
Normal Dose Abdomen	DLIR High	Image quality	5
		Contrast	4
Normal Dose Pelvis	ASIR-V60%	Image quality	4
		Contrast	4
Normal Dose Pelvis	ASIR-V90%	Image quality	4
		Contrast	3

Normal Dose Pelvis	DLIR High	Image quality	4
		Contrast	4
Low Dose Chest	ASIR-V60%	Image quality	4
		Contrast	4
Low Dose Chest	ASIR-V90%	Image quality	4
		Contrast	4
Low Dose Chest	DLIR High	Image quality	4
		Contrast	4
Low Dose Abdomen	ASIR-V60%	Image quality	3
		Contrast	4
Low Dose Abdomen	ASIR-V90%	Image quality	4
		Contrast	3
Low Dose Abdomen	DLIR High	Image quality	4
		Contrast	4
Low Dose Pelvis	ASIR-V60%	Image quality	3
		Contrast	3
Low Dose Pelvis	ASIR-V90%	Image quality	3
		Contrast	2
Low Dose Pelvis	DLIR High	Image quality	4
		Contrast	4
Ultra Low Dose Chest	ASIR-V60%	Image quality	4
		Contrast	4
Ultra Low Dose Chest	ASIR-V90%	Image quality	4
		Contrast	3
Ultra Low Dose Chest	DLIR High	Image quality	4
		Contrast	4
Ultra Low Dose Abdomen	ASIR-V60%	Image quality	3
		Contrast	4
Ultra Low Dose Abdomen	ASIR-V90%	Image quality	4
		Contrast	3
Ultra Low Dose Abdomen	DLIR High	Image quality	5
		Contrast	4
Ultra Low Dose Pelvis	ASIR-V60%	Image quality	2
		Contrast	3
Ultra Low Dose Pelvis	ASIR-V90%	Image quality	3
		Contrast	2
Ultra Low Dose Pelvis	DLIR High	Image quality	4
		Contrast	3

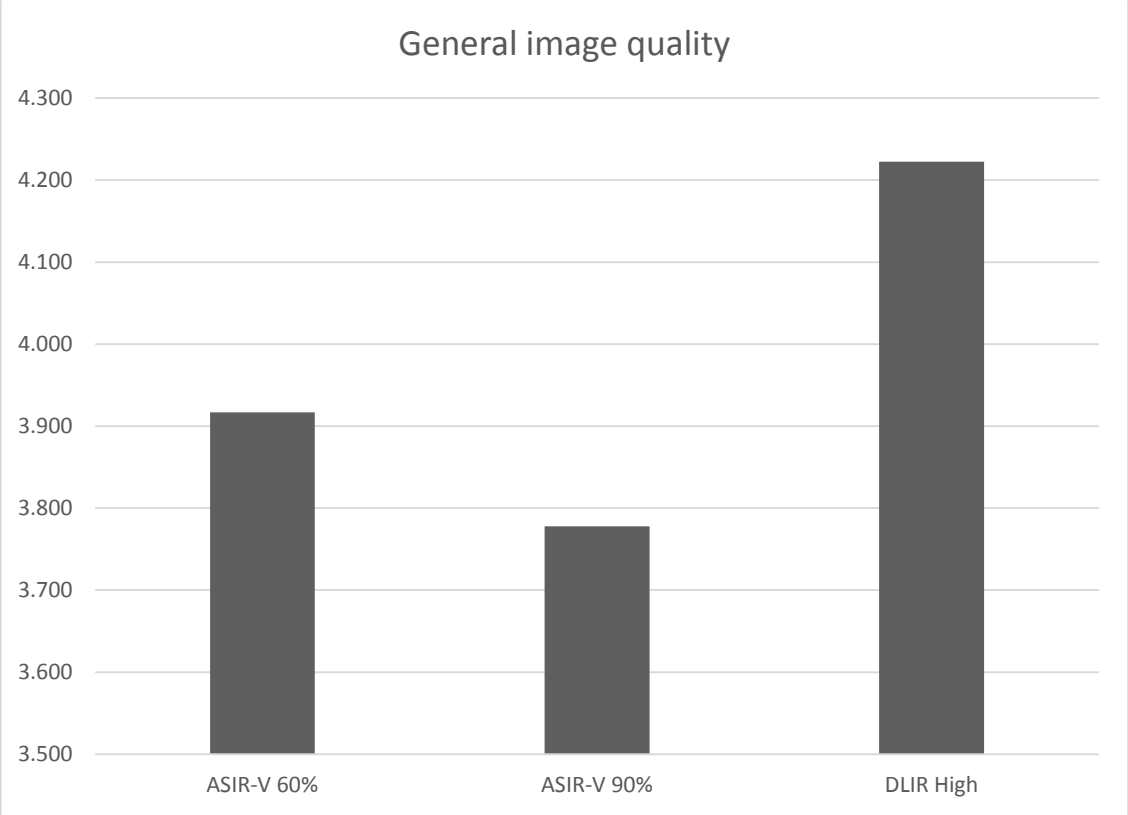

Chart 1: The averages of general image quality scores derived from the qualitative analysis for the CAP region across all dose levels for ASIR-V60%, ASIR-V90% and DLIR High reconstruction algorithms.

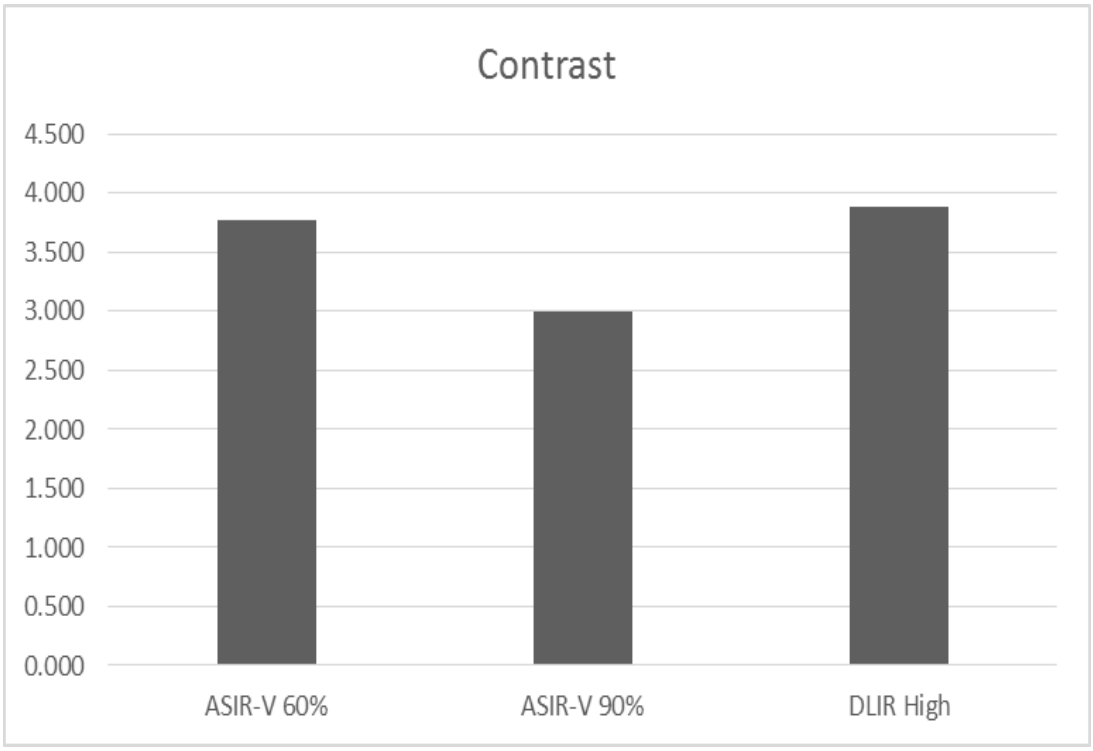

Chart 2: The averages of contrast scores derived from the qualitative analysis for the CAP region across all dose levels for ASIR-V60%, ASIR-V90% and DLIR High reconstruction algorithms.

4. Discussion

4.1 Interpretation of the results

For this study, three similar irradiations were conducted following a standardized protocol known as Chest-Abdomen-Pelvis (CAP). These irradiations utilized varying dose levels on an anthropomorphic phantom to evaluate the capabilities of three reconstruction algorithms: Filtered Back Projection (FBP), Adaptive Statistical Iterative Reconstruction-V (ASIR-V), and Deep Learning Image Reconstruction (DLIR). The first analysis focused on calculating the Signal-to-Noise Ratio (SNR) for distinct regions (chest, abdomen, and pelvis) using predefined regions of interest. Subsequently, a paired test was conducted comparing the SNRs produced by all three reconstruction algorithms across the three dose levels for each specific region. FBP was utilized as the reference algorithm due to its conventional nature among the algorithms considered in the study.

Based on the interpretation of the p-values, when the p-value associated with the Signal-to-Noise Ratio (SNR) comparison between two different images is less than 0.05, it indicates no statistically significant difference in noise between these images. Conversely, if the p-value exceeds 0.05, it suggests a higher likelihood that the noise texture between the two compared images is similar. Upon reviewing the results presented in tables 6, 7, and 8, it becomes evident that the observed p-values align with the aforementioned pattern in the following comparisons:

Chest:

- FBP Normal Dose vs ASIR30% Low Dose: p-value=0,70
- FBP Normal Dose vs DLIR-L Low Dose: p-value=0,16
- FBP Normal Dose vs ASIR60% Ultra Low Dose: p-value=0,40
- FBP Normal Dose vs DLIR-M Ultra Low Dose: p-value=0,11

Abdomen:

- FBP Normal Dose vs ASIR30% Low Dose: p-value=0,64

Pelvis:

- FBP Normal Dose vs ASIR30% Normal Dose: p-value= 0,23
- FBP Normal Dose vs FBP Low Dose: p-value= 0,10
- FBP Normal Dose vs ASIR30% Low Dose: p-value= 0,83
- FBP Normal Dose vs ASIR60% Low Dose: p-value= 0,073
- FBP Normal Dose vs DLIR-Low Low Dose: p-value= 0,069
- FBP Normal Dose vs FBP Ultra Low Dose: p-value= 0,87
- FBP Normal Dose vs ASIR30% Ultra Low Dose: p-value= 0,32

- FBP Normal Dose vs ASIR90% Ultra Low Dose: p-value= 0,06
- FBP Normal Dose vs DLIR-Low Ultra Low Dose: p-value= 0,06

The intriguing conclusion drawn from these results is the possibility of generating images with comparable noise levels, but with reduced irradiation compared to those produced by the conventional FBP reconstruction algorithm in a normal dose level protocol. Achieving this entails the utilization of more sophisticated reconstruction algorithms, particularly, for chest region, employing ASIR-V at a 30% level and DLIR at a low level. Moreover, similar outcomes can be achieved using an ultra-low-dose protocol by utilizing ASIR-V at a 60% level and DLIR at a medium level.

In essence, this implies that both low dose and ultra-low dose protocols can be employed to attain similar noise indexes. This can be accomplished for chest region by integrating ASIR-V30% and DLIR Low for low dose protocols, and ASIR-V60% and DLIR M for ultra-low dose protocols, thus maintaining image quality while reducing irradiation.

Similar is achievable with the use of ASIR-V30% at low dose level protocol for the abdomen.

For pelvis, similar outcomes can be achieved by using ASIR-V30%, ASIR-V60% and DLIR-Low with low dose and ultra-low dose level protocol. It is noticed that in pelvis region using ASIR-V30% at normal dose is providing similar noise with FBP at the same dose level. Also, ASIR-V at different levels also providing similar noise, so could be interpreted as no improvement even though a stronger level of the reconstruction algorithm is used. These observations can be interpreted due to the inherent characteristics of the pelvis region, which demands a higher level of irradiation. This heightened demand arises from the presence of a dense concentration of bone tissues within this anatomical area. Consequently, the solid nature of these tissues necessitates a more powerful beam for adequate penetration, distinguishing it from the abdomen and chest regions in terms of irradiation requirements. This is the reason why on the results of qualitative analysis by the radiologist (Table 12) on ultra-low dose levels the scores from 1-5 are far lower than the rest. This serves as an indication that employing the experimentally devised ultra-low dose protocol, particularly for ASIR-V at most levels and for DLIR at Low and Medium levels, poses difficulty in generating high Signal-to-Noise Ratio (SNR) images for the pelvis region.

Nevertheless, in this study the image acquisition protocols used, have stable mA in order to provide comparable measurements. The limitation mentioned for the pelvis region could be overcome by using modulated mA. In this case more parameters should be calculated in order to obtain comparable results and a further future study could be based on that difference.

Further on this study, in the qualitative analysis, images with the highest Signal-to-Noise Ratio (SNR) and Contrast-to-Noise Ratio (CNR) were handpicked for further evaluation, aiming to align them with routine medical assessments. A seasoned

radiologist with 25+ years of expertise examined 27 regions, employing diverse reconstruction methods and varying dose levels. This comprehensive assessment involved chest, upper abdomen, and pelvis images reconstructed using ASIR60%, ASIR90%, and DLIR High across Normal, Low, and Ultra Low dose levels.

A similar analysis with paired tests was conducted between these three reconstruction algorithms at all three dose levels with ASIR-V60% to be the reference, as the most efficient and most common use. The p-values arising follows the same interpretations with the one explained above. By reviewing the results on Tables 9, 10 and 11 the cases where p-value exceeds 0.05 which suggests a higher likelihood that the noise texture between the two compared images is similar are:

Chest

- ASIR-V60% Normal Dose vs ASIR-V90% Low Dose: p-value=0,53
- ASIR-V60% Normal Dose vs DLIR-H Low Dose: p-value=0,21
- ASIR-V60% Normal Dose vs ASIR-V90% Ultra Low Dose: p-value=0,05
- ASIR-V60% Normal Dose vs DLIR-H Ultra Low Dose: p-value=0,19

Abdomen

- ASIR60 Normal Dose vs ASIR90 Low Dose: p-value=0,056
- ASIR60 Normal Dose vs ASIR90 Ultra Low Dose: p-value=0,94

Pelvis

- All p-values at Table 11 of the paired test exceed 0,05

The results obtained for the pelvis region exhibit similar limitations as those previously elucidated. The notable high correspondence observed in the paired images subjected to testing is primarily attributed to the pervasive issue of poor image quality inherent to the anatomical complexities of the pelvis region.

The findings suggest the potential of ASIR-V at its highest levels, notably 90%, used in this study, to achieve noise suppression comparable to deep learning-based image reconstruction algorithms. To clarify this observation, qualitative analysis, as depicted in Table 12 and Chart 2, reveals lower scores for ASIR-V90% in contrast (21% less than ASIR-V60% and 30% less than DLIR High) and general image quality (4% less than ASIR-V60% and 12% less than DLIR High). Additionally, the radiologist commented on ASIR-V90%, highlighting its tendency to alter imaging texture significantly. They noted a substantial departure from realistic anatomy, resulting in an artificial appearance in the reconstructed images. So, we safely conclude that even ASIR-V90% shows high performance, its diagnostic value is limited as it causes alterations in imaging.

Last but not least, a notable comment radiologist did during the qualitative analysis is that ASIR-V60%, ASIR-V90% and DLIR-H are showing similar performance at all three dose levels. The potential for interpretation arises due to the utilization of a

CAP protocol within this study, where among the three anatomical regions examined, the chest exhibits the least irradiation demand. Additionally, the tube current remains stable throughout the scanning process without modulation. If the tube current were subject to modulation through an automatic exposure control system utilizing scout information, it is conceivable that the chest region would receive insufficient irradiation in comparison to the other regions, potentially leading to divergent imaging results for the three most efficient reconstruction algorithms upon assessment.

4.2 Comparison with current literature, weaknesses of the study and future potentials

According to current literature, there are plenty of publications claim that deep learning-based image reconstruction algorithm are able to improve image quality in various scenarios and for various body regions and also reduce dose by maintaining the image quality. [37] [38] [40] [41] [42] [46] [47]

Specifically, Yang et al., (2023) [37] mention that DLIR exhibited superior image quality and noise texture in both phantom and clinical studies when contrasted with FBP and ASiR-V, and in low-dose radiation abdominal CT scans, DLIR in Medium level consistently upheld the highest image quality and enhanced confidence in diagnosing lesions which was not highlighted in the present investigation. In the abdominal imaging context, another survey by J. E. Lee et al. (2021) [38] outlines that among the DLIR-reconstructed datasets, image quality was optimal at the medium strength level, followed by low and high strengths. In the same study, is highlighted that DLIR algorithms significantly reduced radiation doses by 65.5% to 68.1% compared to the reference image, while preserving similar image quality. Moreover, employing the medium-strength DLIR algorithm produced even better image quality than the reference image, achieving a lowered radiation dose of 36.2% to 50.0%.

In contrast to this study, which employed a generalized CAP protocol applicable to multiple clinical scenarios, a majority of studies are focusing on assessing the impact of DLIR in specific body regions and/or for particular pathologies. A study that appeals to the perspective of this study, in terms of investigated body region, is that of Y. Noda et al. (2021) [39]who assess the image clarity and ability to detect lesions in low-dose whole-body CT during the portal venous phase by employing DLIR. The outcome of this study is DLIR facilitates an approximately 80% decrease in radiation exposure while preserving both image quality and the capability to detect lesions, in comparison to conventional whole-body CT scans at standard doses. The most important difference of this study with the one of Y. Noda et al. (2021) [39] is that the current is based on qualitative and quantitative results instead of only qualitative.

The current literature exhibits a significant focus on thoracic studies involving the utilization of DLIR. Some interesting studies focusing on that is A. Svalkvist et al (2023) [40], J.-M. Jiang, et al (2022) [41] and J. H. Kim, et al (2021) [42]. All of these studies highlight the potential to enhance image quality, reduce noise, and boost diagnostic confidence across various imaging scenarios, including low-dose protocols and lung cancer screening by using deep learning-based image reconstruction.

A study conducted by K. Zhang et al. (2022) [43] utilized an anthropomorphic phantom, specifically the PBU-70, akin to the one employed in the present study. Similar analytical methodologies were applied in both studies for comparative analysis.

Another comprehensive phantom/patient study by Y. Li et al. (2022) [44] proposing low dose CT by leveraging deep learning-based image reconstruction algorithm for osteoporosis screening.

Finally, a comprehensive study conducted by D. Racine et al. (2020) [45] employed a similar protocol configuration to the present study, establishing three dose levels (normal, low, and ultra-low dose). However, this study compared fewer ASIR-V levels (ASIR-V 0%, 50%, and 100% instead of 0%, 30%, 60%, and 90%) yet utilized more intricate and comprehensive metrics compared to the current study. Notably, another distinction lies in the use of an anthropomorphic phantom in the current study and an improvised one in the other study.

The limitations of the current study have been delineated, primarily concerning protocol configuration and the relatively unsophisticated nature of employed metrics. Specifically, aside from qualitative analysis, this study relied on SNR and CNR as metrics. Future research could benefit from employing more sophisticated metrics related to those used in similar studies. Nonetheless, this research stands out from much of the existing literature due to its utilization of an anthropomorphic phantom to simulate a CAP protocol, widely employed in clinical practice for investigating diverse pathologies [35]. Additionally, it introduced an ultra-low-dose protocol, distinguishing it from prior studies.

5. Conclusions

The aim of this study is to evaluate the influence of deep learning-based reconstruction (DLIR) on image quality at three different dose levels (normal, low and ultra-low dose level) within CAP region on a 512-slice CT scanner using a sophisticated anthropomorphic phantom. During the study, FBP considered as conventional reconstructions algorithm and compared with ASIR-V and DLIR for each region and for every distinct dose level. The findings delineate that the employment of ASIR-V and DLIR reconstruction algorithms yields images of equivalent or superior quality while operating at reduced dosage levels. Furthermore, ASIR-V60%, which is the most widely used ASIR-V level, compared with ASIR-V90% and DLIR High which seemed to be the most efficient algorithm. This assessment was complemented by an additional quantitative analysis and a qualitative analysis executed by a radiologist possessing over 25 years of experience. Both sets of findings indicate that DLIR High stands out as the most efficient reconstruction algorithm, capable of reducing dosage while sustaining image quality at levels comparable to ASIR-V60%. Conversely, although ASIR-V90% exhibited satisfactory performance, it demonstrated diminished contrast and realism in image texture. All these findings are consistent with existing literature and additionally suggest the possibility of implementing an experimental ultra-low-dose protocol for CAP. This could be achieved through the application of a deep-learning-based image reconstruction algorithm, maintaining acceptable levels of image quality and contrast akin to those observed in regular and low-dose protocols utilizing conventional reconstruction algorithms. Future studies might consider a similar framework but incorporate protocols with modulated mA settings to enable clearer visualization of the pelvis, which is challenging to image adequately using ultra-low-dose protocols with fixed tube current. Additionally, conducting a more comprehensive investigation involving the utilization of more sophisticated metrics could further enhance the depth and precision of subsequent studies in this domain. These potential avenues could significantly contribute to advancing our understanding and application of imaging protocols in this field.

References

[1] November 8, 1895: Roentgen's Discovery of X-Rays'. Accessed: Feb. 17, 2024. [Online]. Available: http://www.aps.org/publications/apsnews/200111/history.cfm

[2] O. Taubmann, M. Berger, M. Bögel, Y. Xia, M. Balda, and A. Maier, 'Computed Tomography', in *Medical Imaging Systems: An Introductory Guide*, A. Maier, S. Steidl, V. Christlein, and J. Hornegger, Eds., Cham (CH): Springer, 2018. Accessed: Feb. 14, 2024. [Online]. Available: http://www.ncbi.nlm.nih.gov/books/NBK546157/

[3] 'EMI CT Brain Scanner | Science Museum Group Collection'. Accessed: Feb. 13, 2024. [Online]. Available: https://collection.sciencemuseumgroup.org.uk/objects/co134790/emi-ct-brain-scanner-ct-scanner

[4] J. Hsieh and T. Flohr, 'Computed tomography recent history and future perspectives', *J Med Imaging (Bellingham)*, vol. 8, no. 5, p. 052109, Sep. 2021, doi: 10.1117/1.JMI.8.5.052109.

[5] W. A. Kalender, W. Seissler, E. Klotz, and P. Vock, 'Spiral volumetric CT with single-breath-hold technique, continuous transport, and continuous scanner rotation', *Radiology*, vol. 176, no. 1, pp. 181–183, Jul. 1990, doi: 10.1148/radiology.176.1.2353088.

[6] C. R. Crawford and K. F. King, 'Computed tomography scanning with simultaneous patient translation', *Med Phys*, vol. 17, no. 6, pp. 967–982, 1990, doi: 10.1118/1.596464.

[7] A. Luke, K. Shetty, S. Satish, and K. Kilaru, 'Comparison of Spiral Computed Tomography and Cone-Beam Computed Tomography', *J Indian Acad Oral Med Radiol*, vol. 25, no. 3, p. 173, 2013, doi: 10.4103/0972-1363.161096.

[8] 'Comparison of radiation dose and image quality between sequential and spiral brain CT', 2018. Accessed: Feb. 17, 2024. [Online]. Available: https://www.semanticscholar.org/paper/Comparison-of-radiation-dose-and-image-quality-and/c854ef14784cafd93738b50c1995b355f91e4fe6

[9] D. Esses, A. Birnbaum, P. Bijur, S. Shah, A. Gleyzer, and E. J. Gallagher, 'Ability of CT to alter decision making in elderly patients with acute abdominal

pain', *Am J Emerg Med*, vol. 22, no. 4, pp. 270–272, Jul. 2004, doi: 10.1016/j.ajem.2004.04.004.

[10] Z. Y. Zu *et al.*, 'Coronavirus Disease 2019 (COVID-19): A Perspective from China', *Radiology*, vol. 296, no. 2, pp. E15–E25, Aug. 2020, doi: 10.1148/radiol.2020200490.

[11] Z. Y. Zu *et al.*, 'Coronavirus Disease 2019 (COVID-19): A Perspective from China', *Radiology*, vol. 296, no. 2, pp. E15–E25, Aug. 2020, doi: 10.1148/radiol.2020200490

[12] S. P. Power, F. Moloney, M. Twomey, K. James, O. J. O'Connor, and M. M. Maher, 'Computed tomography and patient risk: Facts, perceptions and uncertainties', World J Radiol, vol. 8, no. 12, pp. 902–915, Dec. 2016, doi: 10.4329/wjr.v8.i12.902.

[13] C. for D. and R. Health, 'What are the Radiation Risks from CT?', FDA, Mar. 2018, Accessed: Oct. 04, 2023. [Online]. Available: https://www.fda.gov/radiation-emitting-products/medical-x-ray-imaging/what-are-radiation-risks-ct

[14] C.-F. Cao *et al.*, 'CT Scans and Cancer Risks: A Systematic Review and Dose-response Meta-analysis', *BMC Cancer*, vol. 22, p. 1238, Nov. 2022, doi: 10.1186/s12885-022-10310-2.

[15] N. R. Council, D. on E. and L. Studies, C. on L. Sciences, and C. on the B. E. of I. R. (BEIR V), *Health Effects of Exposure to Low Levels of Ionizing Radiation: BEIR V*. National Academies, 1990.

[16] 'Ionizing radiation and health effects'. Accessed: Oct. 05, 2023. [Online]. Available: https://www.who.int/news-room/fact-sheets/detail/ionizing-radiation-and-health-effects

[17] R. S. of N. A. (RSNA) and A. C. of Radiology (ACR), 'Radiation Dose', Radiologyinfo.org. Accessed: Oct. 05, 2023. [Online]. Available: https://www.radiologyinfo.org/en/info/safety-xray

[18] N. Frane and A. Bitterman, 'Radiation Safety and Protection', in *StatPearls*, Treasure Island (FL): StatPearls Publishing, 2023. Accessed: Oct. 07, 2023. [Online]. Available: http://www.ncbi.nlm.nih.gov/books/NBK557499/

[19] R. A. J. Nievelstein, I. M. van Dam, and A. J. van der Molen, 'Multidetector CT in children: current concepts and dose reduction strategies', *Pediatr Radiol*, vol. 40, no. 8, pp. 1324–1344, Aug. 2010, doi: 10.1007/s00247-010-1714-7

[20] I. Oshina and J. Spigulis, 'Beer–Lambert law for optical tissue diagnostics: current state of the art and the main limitations', *J Biomed Opt*, vol. 26, no. 10, p. 100901, Oct. 2021, doi: 10.1117/1.JBO.26.10.100901

[21] R. Schofield *et al.*, 'Image reconstruction: Part 1 – understanding filtered back projection, noise and image acquisition', *Journal of Cardiovascular Computed Tomography*, vol. 14, no. 3, pp. 219–225, May 2020, doi: 10.1016/j.jcct.2019.04.008.

[22] G. L. Zeng, 'Fast filtered backprojection algorithm for low-dose computed tomography', *J Radiol Imaging*, vol. 4, no. 7, pp. 45–50, Dec. 2020, doi: 10.14312/2399-8172.2020-7.

[23] D. Qiu and E. Seeram, 'Does Iterative Reconstruction Improve Image Quality and Reduce Dose in Computed Tomography?', *Radiology - Open Journal*, vol. 1, pp. 42–54, Sep. 2016, doi: 10.17140/ROJ-1-108.

[24] J. A. Seibert, 'Iterative reconstruction: how it works, how to apply it', *Pediatr Radiol*, vol. 44 Suppl 3, pp. 431–439, Oct. 2014, doi: 10.1007/s00247-014-3102-1.

[25] S. Singh *et al.*, 'Abdominal CT: comparison of adaptive statistical iterative and filtered back projection reconstruction techniques', *Radiology*, vol. 257, no. 2, pp. 373–383, Nov. 2010, doi: 10.1148/radiol.10092212.

[26] H. Kwon *et al.*, 'The adaptive statistical iterative reconstruction-V technique for radiation dose reduction in abdominal CT: comparison with the adaptive statistical iterative reconstruction technique', *Br J Radiol*, vol. 88, no. 1054, p. 20150463, Oct. 2015, doi: 10.1259/bjr.20150463

[27] S. N. Patro, S. Chakraborty, and A. Sheikh, 'The use of adaptive statistical iterative reconstruction (ASiR) technique in evaluation of patients with cervical spine trauma: impact on radiation dose reduction and image quality', *Br J Radiol*, vol. 89, no. 1060, p. 20150082, Apr. 2016, doi: 10.1259/bjr.20150082.

[28] J. Fan, M. Yue, and R. Melnyk, 'Benefits of ASiR-V* Reconstruction for Reducing Patient Radiation Dose and Preserving Diagnostic Quality in CT Exams'.

[29] The future of CT: deep learning reconstruction - Clinical Radiology'. Accessed: Oct. 12, 2023. [Online]. Available: https://www.clinicalradiologyonline.net/article/S0009-9260(21)00067-2/fulltext

[30] D. C. Rotzinger *et al.*, 'Task-Based Model Observer Assessment of A Partial Model-Based Iterative Reconstruction Algorithm in Thoracic Oncologic Multidetector CT', *Sci Rep*, vol. 8, no. 1, Art. no. 1, Dec. 2018, doi: 10.1038/s41598-018-36045-4.

[31] Z. Alagic *et al.*, 'Deep learning versus iterative image reconstruction algorithm

for head CT in trauma', *Emerg Radiol*, vol. 29, no. 2, pp. 339–352, Apr. 2022, doi: 10.1007/s10140-021-02012-2.

[32] S. Despotopoulos, K. Dimos and A. Stratis. *How Low Is the Low Dose? Establishing Deep Learning-based Protocols at Planar Radiography Dose Levels.* EFOMP, Summer 2023 p. 11-14.

[33] C. M. McLeavy *et al.*, 'The future of CT: deep learning reconstruction', *Clinical Radiology*, vol. 76, no. 6, pp. 407–415, Jun. 2021, doi: 10.1016/j.crad.2021.01.010.

[34] C. Arndt, F. Güttler, A. Heinrich, F. Bürckenmeyer, I. Diamantis, and U. Teichgräber, 'Deep Learning CT Image Reconstruction in Clinical Practice', *Rofo*, vol. 193, no. 3, pp. 252–261, Mar. 2021, doi: 10.1055/a-1248-2556.

[35] D. G. Sutton, S. McVey, D. Gentle, A. J. Hince, N. MacDonald, and S. McCallum, 'CT chest abdomen pelvis doses in Scotland: has the DRL had its day?', *Br J Radiol*, vol. 87, no. 1041, p. 20140157, Sep. 2014, doi: 10.1259/bjr.20140157.

[36] K. Zhang and A. B. Aslan, 'AI technologies for education: Recent research & future directions', *Computers and Education: Artificial Intelligence*, vol. 2, p. 100025, Jan. 2021, doi: 10.1016/j.caeai.2021.100025.

[37] C. Yang et al., 'Deep learning image reconstruction algorithms in low-dose radiation abdominal computed tomography: assessment of image quality and lesion diagnostic confidence', Quant Imaging Med Surg, vol. 13, no. 5, pp. 3161–3173, Dec. 2023, doi: 10.21037/qims-22-1227.

[38] J. E. Lee et al., 'The potential for reduced radiation dose from deep learning-based CT image reconstruction: A comparison with filtered back projection and hybrid iterative reconstruction using a phantom', Medicine (Baltimore), vol. 100, no. 19, p. e25814, Dec. 2021, doi: 10.1097/MD.0000000000025814.

[39] Y. Noda et al., 'Low-dose whole-body CT using deep learning image reconstruction: image quality and lesion detection', Br J Radiol, vol. 94, no. 1121, p. 20201329, Dec. 2021, doi: 10.1259/bjr.20201329.

[40] A. Svalkvist et al., 'Evaluation of deep-learning image reconstruction for chest CT examinations at two different dose levels', J Appl Clin Med Phys, vol. 24, no. 3, p. e13871, Mar. 2023, doi: 10.1002/acm2.13871.

[41] J.-M. Jiang, L. Miao, X. Liang, Z.-H. Liu, L. Zhang, and M. Li, 'The Value of Deep Learning Image Reconstruction in Improving the Quality of Low-Dose Chest CT Images', Diagnostics (Basel), vol. 12, no. 10, p. 2560, Oct. 2022, doi: 10.3390/diagnostics12102560.

[42] J. H. Kim, H. J. Yoon, E. Lee, I. Kim, Y. K. Cha, and S. H. Bak, 'Validation of Deep-Learning Image Reconstruction for Low-Dose Chest Computed Tomography Scan: Emphasis on Image Quality and Noise', Korean J Radiol, vol. 22, no. 1, pp. 131–138, Jan. 2021, doi: 10.3348/kjr.2020.0116.

[43] K. Zhang et al., 'Deep learning image reconstruction in pediatric abdominal and chest computed tomography: a comparison of image quality and radiation dose', Quant Imaging Med Surg, vol. 12, no. 6, pp. 3238–3250, Jun. 2022, doi: 10.21037/qims-21-936.

[44] Y. Li et al., 'Deep-learning image reconstruction for image quality evaluation and accurate bone mineral density measurement on quantitative CT: A phantom-patient study', Front Endocrinol (Lausanne), vol. 13, p. 884306, 2022, doi: 10.3389/fendo.2022.884306.

[45] D. Racine et al., 'Task-based characterization of a deep learning image reconstruction and comparison with filtered back-projection and a partial model-based iterative reconstruction in abdominal CT: A phantom study', Physica Medica, vol. 76, pp. 28–37, Aug. 2020, doi: 10.1016/j.ejmp.2020.06.004.

[46] Y. Bie, S. Yang, X. Li, K. Zhao, C. Zhang, and H. Zhong, 'Impact of deep learning-based image reconstruction on image quality and lesion visibility in renal computed tomography at different doses', Quant Imaging Med Surg, vol. 13, no. 4, pp. 2197–2207, Apr. 2023, doi: 10.21037/qims-22-852.

[47] S. Yang et al., 'Impact of novel deep learning image reconstruction algorithm on diagnosis of contrast-enhanced liver computed tomography imaging: Comparing to adaptive statistical iterative reconstruction algorithm', J Xray Sci Technol, vol. 29, no. 6, pp. 1009–1018, 2021, doi: 10.3233/XST-210953.

[48] O. S. Pianykh *et al.*, 'Continuous Learning AI in Radiology: Implementation Principles and Early Applications', *Radiology*, vol. 297, no. 1, pp. 6–14, Oct. 2020, doi: 10.1148/radiol.2020200038.

[49] A. Hosny, C. Parmar, J. Quackenbush, L. H. Schwartz, and H. J. W. L. Aerts, 'Artificial intelligence in radiology', *Nat Rev Cancer*, vol. 18, no. 8, pp. 500–510, Aug. 2018, doi: 10.1038/s41568-018-0016-5.

Appendix

Table 3A:

Chest SNR results

Reconstruction algorithm	Normal Dose SNR	Low Dose SNR	Ultra Low Dose SNR
FBP ROI 1	69,3	64,7	51,0
FBP ROI 2	82,0	67,6	57,6
FBP ROI 3	91,5	73,4	60,6
FBP ROI 4	82,0	71,8	59,5
FBP ROI 5	76,9	61,5	51,6
ASIR-V30% ROI 1	83,8	77,9	60,3
ASIR-V30% ROI 2	102,1	81,1	68,2
ASIR-V30% ROI 3	114,7	89,2	72,4
ASIR-V30% ROI 4	123,5	88,4	70,9
ASIR-V30% ROI 5	95,2	74,4	61,9
ASIR-V60% ROI 1	110,8	100,7	75,4
ASIR-V60% ROI 2	143,4	104,7	86,6
ASIR-V60% ROI 3	163,6	117,6	92,6
ASIR-V60% ROI 4	169,6	120,3	88,6
ASIR-V60% ROI 5	129,8	96,8	79,7
ASIR-V90% ROI 1	151,1	132,9	99,5
ASIR-V90% ROI 2	218,4	147,9	116,8
ASIR-V90% ROI 3	262,6	169,4	133,3
ASIR-V90% ROI 4	256,5	175,2	116,4
ASIR-V90% ROI 5	196,0	136,7	112,0
DLIR-L ROI 1	89,8	81,0	61,8

DLIR-L ROI 2	105,5	88,1	74,2
DLIR-L ROI 3	121,7	98,0	78,7
DLIR-L ROI 4	128,3	97,9	75,2
DLIR-L ROI 5	102,0	79,1	66,0
DLIR-M ROI 1	113,3	104,9	77,7
DLIR-M ROI 2	137,3	110,4	92,9
DLIR-M ROI 3	158,3	128,1	102,0
DLIR-M ROI 4	166,8	129,7	95,3
DLIR-M ROI 5	131,5	103,9	84,4
DLIR-H ROI 1	158,3	144,4	107,0
DLIR-H ROI 2	192,8	154,4	122,3
DLIR-H ROI 3	232,1	185,1	147,0
DLIR-H ROI 4	232,6	192,1	129,9
DLIR-H ROI 5	192,2	142,4	121,6

Table 4A:

Abdomen SNR results

Reconstruction algorithm	**Normal Dose SNR**	**Low Dose SNR**	**Ultra Low Dose SNR**
FBP ROI 1	2,5	2,0	1,7
FBP ROI 2	2,8	2,3	2,1
FBP ROI 3	2,7	2,2	1,7
FBP ROI 4	2,8	2,3	1,9
FBP ROI 5	2,9	1,9	2,0
ASIR-V30% ROI 1	3,2	2,6	2,2
ASIR-V30% ROI 2	3,6	3,0	2,7
ASIR-V30% ROI 3	3,4	2,9	2,1
ASIR-V30% ROI 4	3,6	3,0	2,5

ASIR-V30% ROI 5	3,9	2,5	2,6
ASIR-V60% ROI 1	4,7	3,7	3,1
ASIR-V60% ROI 2	5,1	4,2	3,8
ASIR-V60% ROI 3	4,7	4,2	2,7
ASIR-V60% ROI 4	5,3	4,3	3,7
ASIR-V60% ROI 5	5,9	3,4	3,6
ASIR-V90% ROI 1	7,5	5,7	4,6
ASIR-V90% ROI 2	8,4	6,3	5,8
ASIR-V90% ROI 3	6,7	6,7	3,6
ASIR-V90% ROI 4	8,9	6,9	6,3
ASIR-V90% ROI 5	11,0	4,9	5,6
DLIR-L ROI 1	4,1	3,6	3,3
DLIR-L ROI 2	4,5	4,0	3,8
DLIR-L ROI 3	4,2	4,0	3,2
DLIR-L ROI 4	4,5	3,9	3,6
DLIR-L ROI 5	4,8	3,4	3,8
DLIR-M ROI 1	5,0	4,6	4,3
DLIR-M ROI 2	5,5	5,2	4,9
DLIR-M ROI 3	5,1	5,2	4,1
DLIR-M ROI 4	5,5	5,0	4,5
DLIR-M ROI 5	6,0	4,4	4,9
DLIR-H ROI 1	6,7	6,9	6,2
DLIR-H ROI 2	7,4	7,5	7,4
DLIR-H ROI 3	6,7	7,6	5,8
DLIR-H ROI 4	7,3	7,5	6,7
DLIR-H ROI 5	8,0	6,4	7,0

Table 5A:

Pelvis SNR results

Reconstruction algorithm	Normal Dose SNR	Low Dose SNR	Ultra Low Dose SNR
FBP ROI 1	0,423	0,506	0,763
FBP ROI 2	0,657	0,457	0,761
FBP ROI 3	0,540	0,449	0,604
FBP ROI 4	0,727	0,374	0,307
ASIR-V30% ROI 1	0,517	0,644	0,968
ASIR-V30% ROI 2	0,832	0,595	0,943
ASIR-V30% ROI 3	0,674	0,578	0,736
ASIR-V30% ROI 4	0,930	0,458	0,369
ASIR-V60% ROI 1	0,665	0,863	1,290
ASIR-V60% ROI 2	1,168	0,860	1,240
ASIR-V60% ROI 3	0,897	0,788	0,948
ASIR-V60% ROI 4	1,340	0,611	0,509
ASIR-V90% ROI 1	0,947	1,616	1,948
ASIR-V90% ROI 2	1,758	1,640	1,736
ASIR-V90% ROI 3	1,225	1,150	1,265
ASIR-V90% ROI 4	2,204	0,856	0,688
DLIR-L ROI 1	0,640	0,886	1,265
DLIR-L ROI 2	1,005	0,860	1,170
DLIR-L ROI 3	0,856	0,778	0,965
DLIR-L ROI 4	1,162	0,619	0,540
DLIR-M ROI 1	0,775	1,140	1,536
DLIR-M ROI 2	1,209	1,084	1,426

DLIR-M ROI 3	1,027	1,012	1,198
DLIR-M ROI 4	1,397	0,761	0,702
DLIR-H ROI 1	0,981	1,522	2,062
DLIR-H ROI 2	1,569	1,685	1,867
DLIR-H ROI 3	1,340	1,293	1,583
DLIR-H ROI 4	1,723	1,008	0,900